

SC5076.5FR

AD A057323

AD NO. _____
DDC FILE COPY

① LEVEL

This Document
Reproduced From
Best Available Copy

SC5076.5FR

18

COPY NO. _____

IMPACT DAMAGE IN CARBON COMPOSITES: EFFECT OF MICROSTRUCTURE

FINAL REPORT

by

A. G. Evans, M. Metcalf
W. F. Adler, L. J. Hageman
and G. Gurtman

Submitted to:

Office of Naval Research
800 N. Quincy Road
Arlington, VA

Final Report

5/1/76 - 4/30/78

DDC
RECEIVED
AUG 10 1978
B

This Research was Sponsored by the Office of Naval Research
Under Contract No. N00014-76-C-0854 (Project No. 471 - NR032-570)

Approved for Public Release; distribution unlimited



Rockwell International

Science Center

78 07 28 016

UNCLASSIFIED

SECURITY CLASSIFICATION OF THIS PAGE (When Data Entered)

REPORT DOCUMENTATION PAGE		READ INSTRUCTIONS BEFORE COMPLETING FORM
1. REPORT NUMBER	2. GOVT ACCESSION NO.	3. RECIPIENT'S CATALOG NUMBER
4. TITLE (and Subtitle) ⑥ IMPACT DAMAGE IN CARBON COMPOSITES: EFFECTS OF MICROSTRUCTURE		5. TYPE OF REPORT & PERIOD COVERED Final Report 5/01/76 thru 04/30/78
7. AUTHOR(S) ⑩ A. G. Evans, M. Metcalf, W. F. Adler, L. J. Hageman G. Gurtman		6. PERFORMING ORG. REPORT NUMBER ⑪ SC5076-5FR ^Y
9. PERFORMING ORGANIZATION NAME AND ADDRESS Rockwell International Science Center Thousand Oaks, CA 91350		8. CONTRACT OR GRANT NUMBER(s) ⑬ N00014-76-C-0854 ^Y
11. CONTROLLING OFFICE NAME AND ADDRESS Office of Naval Research 800 N. Quincy Street Arlington, VA 22217 ⑪ 6 Jul 78		10. PROGRAM ELEMENT, PROJECT, TASK AREA & WORK UNIT NUMBERS 471 (NR032-570)
14. MONITORING AGENCY NAME & ADDRESS (if different from Controlling Office) ⑫ 80 P.		12. REPORT DATE July 6, 1978
		13. NUMBER OF PAGES 74
		15. SECURITY CLASS. (of this report) Unclassified
		15a. DECLASSIFICATION/DOWNGRADING SCHEDULE
16. DISTRIBUTION STATEMENT (of this Report) Approved for Public Release; distribution unlimited		
17. DISTRIBUTION STATEMENT (of the abstract entered in Block 60, if different from Report) ⑨ Final Rept. 1 May 76-30 Apr 78		
18. SUPPLEMENTARY NOTES		
19. KEY WORDS (Continue on reverse side if necessary and identify by block number) carbon composites, kink formation, erosion, matrix yield strength, fiber fracture, impact damage		
20. ABSTRACT (Continue on reverse side if necessary and identify by block number) The penetration damage created in carbon composites with a range of microstructures has been characterized for both quasi-static and dynamic conditions. Several quasi-static properties of the composites have also been measured. Analyses of the quasi-static penetration have been developed, which appear to present a consistent interpretation of the damage and its relation to the quasi-static properties. A preliminary numerical computation of the dynamic damage has been conducted, with encouraging results. Suggestions for microstructural modifications that should enhance the damage resistance have		

DD FORM 1 JAN 73 1473 EDITION OF 1 NOV 68 IS OBSOLETE

UNCLASSIFIED

SECURITY CLASSIFICATION OF THIS PAGE (When Data Entered)

389 949

alt.

UNCLASSIFIED

SECURITY CLASSIFICATION OF THIS PAGE(When Data Entered)

been made, based on the results of both the observations and analyses.

ACCESS	
INFO	<input checked="" type="checkbox"/>
DIS	<input type="checkbox"/>
...	<input type="checkbox"/>
DIS	
SPECIAL	
A	

UNCLASSIFIED

SECURITY CLASSIFICATION OF THIS PAGE(When Data Entered)



Rockwell International
Science Center

SC5076.5FR

IMPACT DAMAGE IN CARBON COMPOSITES:
EFFECTS OF MICROSTRUCTURE

By:

A. G. Evans and M. Metcalf

Science Center, Rockwell International
Thousand Oaks, California 91360

W. F. Adler

Effects Technology, Inc.
Santa Barbara, California 93111

L. J. Hageman and G. Gurtman

Systems, Science and Software
La Jolla, California 92409

78 07 28 016



SC5076.5FR

ABSTRACT

The penetration damage created in carbon composites with a range of microstructures has been characterized for both quasi-static and dynamic conditions. Several quasi-static properties of the composites have also been measured. Analyses of the quasi-static penetration have been developed, which appear to present a consistent interpretation of the damage and its relation to the quasi-static properties. A preliminary numerical computation of the dynamic damage has been conducted, with encouraging results. Suggestions for microstructural modifications that should enhance the damage resistance have been made, based on the results of both the observations and analyses.



TABLE OF CONTENTS

	<u>Page</u>
1.0 INTRODUCTION.....	1
2.0 MATERIALS.....	2
3.0 QUASI-STATIC TESTS.....	3
3.1 Constituent Moduli.....	3
3.2 Constrained Compression Tests.....	4
3.3 Penetration Tests.....	7
3.4 Damage Interpretation.....	10
4.0 IMPACT TESTS.....	15
4.1 Test Techniques.....	15
4.2 Damage Characterization.....	15
4.3 Damage Interpretation.....	17
5.0 NUMERICAL CALCULATION OF KINKING.....	19
5.1 Computational Scheme.....	19
5.2 Results.....	22
6.0 SUMMARY.....	23
APPENDIX I.....	26
APPENDIX II.....	32
APPENDIX III.....	34
REFERENCES.....	42
TABLES.....	44
FIGURES.....	50



SC5076.5FR

1.0 INTRODUCTION

Studies of the damage in carbon composites created by the impact of projectiles have identified kinking as a primary damage mechanism.^(1,2) The presence of kinks below and adjacent to the impact crater (Fig. 1) apparently degrades the mechanical strength of the material, and permits ready ejection of the kinked zone upon subsequent impact. The characterization and interpretation of the microstructural dependence of the kink zone thus has important implications for the design of composites with superior impact damage and erosion resistance.

The present study addresses the microstructural issue by examining the projectile damage created in carbon composites with a range of microstructures. The complexity of impact damage problems is recognized and has been described in some detail for carbon-carbon composites.⁽¹⁾ In consequence, following an approach adopted for the analysis of impact damage in isotropic brittle materials, a series of carefully selected quasi-static studies are firstly performed and analyzed, to provide a qualitative perspective from which the impact problem can be viewed. The quasi-static studies include compression tests designed to examine kink initiation, compliance tests to assess the constituent properties, and penetration tests to determine the dynamic penetration resistance.

The quasi-static studies are followed by projectile impact tests, which characterize the extent of kinking and its dependence on microstructure. A sample numerical calculation is then presented which indicates an approach for analyzing the impact damage phenomenon in detail. Finally, the implications of the study for both the development of simple



SC5076.5FR

damage characterization tests and for the fabrication of materials with an improved damage resistance are discussed.

2.0 MATERIALS

Carbon composites of the type considered in this paper consist of bundles of carbon fibers, arranged in an orthogonal interpenetrating network, disposed in a matrix of graphite. The graphite thus exists as interfiber material within the bundles and as isolated interstices between bundles.⁽³⁾ The graphite matrix invariably contains porosity and often the interstices are separated from one (or more) of the adjacent bundles.⁽³⁾ A proportion of the individual fibers within the bundles are fractured, at statistically distributed locations; frequently, regions of considerable fiber distortion are in evidence.⁽³⁾ The role of these microstructural inhomogeneities is an important theme of this paper.

The characteristics of the materials selected for detailed study are summarized in Table I. The rationale for selecting these materials was based on the premise that damage trends could be most effectively deduced if the microstructural (bundle and interstice) dimensions and the properties of the constituents (fibers and matrix) could be independently varied. Consequently, materials A, B, and C are observed to have similar relative bundle areas, but different constituents; while materials C, D, and E have similar constituents but different bundle areas.



3.0 QUASI-STATIC TESTS

Previous studies^(3,4) have indicated that kinking can occur when the fiber bundles are subjected to longitudinal compression, lateral shear or lateral compression: each mode being prevalent in impacted samples. The available analyses of these kink formation processes,⁽³⁻⁶⁾ although capable of rationalizing certain aspects of kink formation, are still too rudimentary to predict kink initiation conditions. An experimental measurement is thus required. A constrained compression test designed to provide this information is described in this section. The interpretation of the test results invokes analyses of compressive bundle deformation, described in Appendix I, and of kink initiation, described in Appendix II.

The penetration resistance afforded by a particular microstructure is related in some complex fashion to the kinking process, and other mechanisms of deformation. A measure of the penetration resistance is obtained by performing penetration tests, and some of the controlling parameters are elucidated by examining the damage surrounding the penetration zone. A damage analysis is also undertaken, to provide insights pertinent to the impact damage problem. The analysis utilizes approximate relations for the deformation that accompanies penetration, developed in Appendix III.

3.1 CONSTITUENT MODULI

The elastic and plastic properties of the microstructural constituents are important parameters for all impact damage models. A series of microcompression tests have been designed to obtain approximate values of these important properties. The values are necessarily approximate in



character because each property is derived from uniaxial force/displacement curves (compliance curves) by assuming elastic isotropy. More precise measurements of the individual constituent properties will ultimately be needed. However, this is a nontrivial problem; which is not attempted in the present study, since the current objective is to obtain a measure of the relative trends in these properties with microstructure.

An in-situ compliance measurement technique has been described previously,⁽³⁾ and provides values for the constituent properties summarized in Table II. In this study, the in-situ tests were augmented by individual compressive compliance tests on small sections of each microstructural constituent. The constituents were isolated using a precision dicing saw and compression tests conducted on a small Instron machine (with 0.1 kg load cell), using an LVTD clip gauge device to monitor the displacement of the sample. The results are summarized in Table II. It is apparent that the two methods yield comparable results.

3.2 CONSTRAINED COMPRESSION TESTS

A quasi-static technique for measuring the onset conditions for kinking under longitudinal compression has been devised. The technique (Fig. 2a) involves the application of equal steady state compressive constraints in two orthogonal directions, with a monotonically increasing compression applied in the third orthogonal direction. The use of constraints is important because this ensures that the damage, when it initiates, occurs as kinks (Fig. 3): rather than bundle fracture, fiber/matrix debonding, etc., which frequently occur in the absence of constraint. The apparatus used for



this experiment is depicted in Fig. 2b. The constraints are applied through mechanical screw devices, and the magnitudes of the forces applied to the composite are measured using strain gauges attached to the compression blocks. The orthogonal compression is applied, through a self aligning cylindrical plunger, by a rigid constant displacement rate device (e.g., an Instron testing machine). The load and displacement are recorded using conventional load cell and displacement gauge (LVDT) instrumentation.

A typical load displacement behavior obtained under constrained compression is shown in Fig. 4. Initially, the load increases linearly with displacement. Subsequently, there is a small load decrement (yield point), followed by a nonlinear increase in load (to a load maximum). Sectioning of samples tested to various locations on the load/deflection curve indicates that there is no detectable damage in the linear region. However, immediately above the load discontinuity, a kink is invariably detected in one of the longitudinal bundles (Fig. 3). It is presumed, therefore, that this discontinuity is associated with the onset of longitudinal bundle kinking. At larger loads, well into the nonlinear region (Fig. 4), complex kinking of the lateral bundles is first discerned.

Critical values of the kink initiation conditions are obtained from the load discontinuity, for each of the materials listed in Table I. The critical kink initiation stresses are obtained from the applied strain at yield and the approximate moduli of the bundles and matrix (Table II). The critical stresses are plotted on Fig. 5. For the three materials (A,B,C) with relatively isotropic bundle dimensions, the critical stresses σ_c^k are independent of the constraint. However, σ_c^k increases with increase in



SC5076.5FR

constraint for the two materials with a predominance of longitudinal bundles (D,E). Sectioning of these samples after testing indicated that the lateral bundles in the latter two samples had been extensively kinked by the constraining loads (thereby, enabling the constraints to be transmitted to the longitudinal bundles).

The results obtained at the minimum constraint (~ 15 MPa) are replotted in Fig. 6 in terms of the cumulative kink initiation probability, $\Phi(\sigma^C)$, obtained from order statistics.

Kink formation under axial compression is associated with the presence of inhomogeneities within the bundles (Appendix I). The involvement of inhomogeneities has statistical implications for the kink initiation stress, reminiscent of the statistics of brittle fracture.⁽⁷⁾ Specifically, for a spatially random distribution of inhomogeneities, the probability, ϕ , of kink initiation in a small element of bundle, length Δl and cross section A_b , is

$$\phi = A_b \Delta l \int_0^{\sigma} g(S_k) dS_k$$

where $g(S_k) dS_k$ is the number of inhomogeneities in unit volume of bundle that produce kinks at applied axial compressive stresses between S_k and $S_k + dS_k$, and σ is the level of the applied compression. Then, if there is no interaction between inhomogeneities, the probability of kink initiation in bundles of total length l can be obtained from the product of the survival probabilities of each element, as:



$$\Phi(\sigma_c^k) = 1 - \sum_1^{l/\Delta l} (1 - \phi) \approx 1 - \exp \left[-A_b \int_l d\ell \int_0^{\sigma_c^k} g(S_k) dS_k \right] \quad (2)$$

For the present tests, the applied stress is uniform and Eq. (2) reduces to:

$$\xi - \ln \left[1 - \Phi(\sigma_c^k) \right] = A_b \ell \int_0^{\sigma_c^k} g(S_k) dS_k \quad (3)$$

The function $g(S_k)$ can also be expressed in terms of ξ , obtained by direct inversion of Eq. (3), as:

$$g(S_k) = (d\xi/dS_k)/A_b \ell \quad (4)$$

The values of $g(S_k)$, obtained from a polynomial fit of the data in Fig. 6, are plotted in Fig. 7. It is apparent from Fig. 7 that a suitable function for $g(S_k)$ is;

$$g(S_k) = \lambda (S_k/S^*)^k \quad (5)$$

where k is a shape parameter, S^* is a scale parameter, and λ is a constant. The specific values of k , S^* and λ pertinent to each material are indicated on Fig. 7. These values of $g(S_k)$ can hereafter be inserted into Eq. (2) to obtain kink initiation probabilities for inhomogeneous axial deformation.

3.3 PENETRATION TESTS

An instrumented drop tower was used for the penetration tests⁽⁸⁾ (this test might be considered dynamic because it involves penetration



SC5076.5FR

velocities of a few meters per second, four orders of magnitude greater than conventional static loading rates). By directly instrumenting the penetrator, reasonably accurate simultaneous measurements of the load and deflection could be obtained. A deflection gauge system was used for penetration measurements. Two Biomation Model 802 Transient Records were used to record load and deflection signals. The records were synchronized by a Tetrax FG 501 Function Generator. The information was digitized, fed into a Hewlett-Packard Model 9830A computer, and stored on magnetic tape. The raw data could then be plotted or further processed. The final result is a plot of penetration pressure, p , versus depth of penetration q/r_j (normalized to the indenter radius r_j). A curve fitting procedure defined by

$$p = p_0 (q/2r_j)^n \quad (6)$$

was then applied to the data. The coefficient p_0 is the pressure at one diameter of penetration, while the exponent n is the slope of the pressure/penetration curve (related to the work hardening exponent). The parameters p_0 and n are determined by a least mean squares fit. Penetration pressures, p_0 , and work hardening exponents are obtained for each material and summarized in Table III.

The damage in the penetration samples was characterized optically, after sectioning through the penetration zone and polishing. The damage obtained with a relatively large (3 mm diameter) penetrator is summarized in Figs. 8 and 9. The damage in the longitudinal bundles has several important features (Fig. 8). The kinking in the bundles beneath the impact crater (bundles C and D, and B, E, F below lateral bundle 3) appears to exhibit



SC5076.5FR

little spatial correlation, either along the bundles or between adjacent bundles. Kink pairs of opposite sign appear to be the primary mechanism for retaining the initial bundle alignment. The kinks at the extremity of the damage zone generally form at inhomogeneities, as indicated on the figure. The kinking in the bundles beside the crater (bundles B and F) tend to exhibit a uniform spatial separation, with the kinks usually initiating near the corners of an out-of-plane lateral bundle (e.g., 1b, 2b, 1f, 2f, and 3f). The kink separation is thus approximately equal to the diameter of a lateral bundle plus a matrix interstice. Also, the kinks tend to conform to a single orientation. Finally, it is noted that kinks occasionally occur in bundles that are not directly subject to interaction with the penetrator (e.g., bundle A).

The damage to the in-plane lateral bundles also has important implications (Fig. 9). The lateral extent of the kinks in the bundles beside the crater is restricted to less than a few bundle diameters. Usually, these kinks are highly correlated, initiating from the corners of out-of-plane lateral fiber bundles along a single plane. It is instructive to regard these kinks as being induced by a shear displacement as depicted by the vectors in Fig. 9. Complex kinks usually appear directly beneath the impact center and occasional fractures occur in the same vicinity (Fig. 9).

The depth of the kink zone in the longitudinal bundles depends on both the diameter of the penetrator and the penetration rate. The depths below the crater measured for a 1 mm diameter penetrator are summarized in Table III and on Fig. 16.



3.4 DAMAGE INTERPRETATION

3.4.1 Compression Tests

The kink initiation stresses obtained in the compression tests can be rationalized in terms of the enhanced curvature produced by an applied compression at local inhomogeneities (Appendix I), coupled with the critical kink formation conditions (Appendix II). The fiber curvatures that result from an applied compression depend most prominently on the initial dimensions (\hat{y}, \hat{z}) of the inhomogeneity (Appendix I), although the matrix yield strength and lateral bundle modulus can also be significant. The fiber curvatures generate local tensile stresses, which are the driving force for kink initiation. The magnitude of the tensile stress required to initiate kinking is typically influenced by the matrix yield strength (Appendix II) with the fiber fracture strength and modulus also being important in certain regimes. The critical applied compression for kink formation should thus be primarily influenced by the inhomogeneity dimensions and the matrix yield strength, with the constituent moduli and fiber fracture strength as possible alternatives. The trends in the kink initiation stress are broadly interpreted in terms of these influences.

The relatively invariant kink formation stress σ_c^k (at low constraints) obtained for the three materials containing the same fiber and matrix constituents (C,D,E) indicates that there are no unexpected influences of the bundle dimensions. The elevation of σ_c^k by lateral constraint (Fig. 5), when this constraint is transmitted to the longitudinal bundles, can be interpreted as resulting from a suppression of matrix yield (i.e., through



a Von Mises criterion, Eq. (12)) or perhaps a decrease in the initial amplitude \hat{y} of inhomogeneities. This would suggest a criterion for kink formation that depends on the difference $\Delta\sigma$ between the maximum σ_{\max} and minimum σ_{\min} compressive stress (i.e., the shear stress). Additional work is needed to establish the detailed nature of this criterion; although studies on uniaxial carbon/epoxy composites⁽⁶⁾ infer a direct proportionality ($\Delta\sigma \propto \sigma_c^k$). For purposes of further analysis it is thus assumed that kinking initiates when σ_c^k is equal to the measured kink initiation stress at zero constraint (Figs. 5, 6).

The strong effects of the fiber and matrix properties on the kink initiation stress (materials A, B, C) are of great significance. Inspection of the material microstructures (cf. Figs. 11 and 12) indicates that the fibers in materials A and B exhibit more extensive perturbations from linearity than in material C, since only in the latter can individual fibers be traced for significant distances on a planar section. Also, the latter has a much reduced density of voids, both within the bundles and within the interstices, accounting for its greater yield strength (Table II). The superior material (C) is thus characterized by a reduced size distribution of inhomogeneities (smaller \hat{y}) and a larger matrix yield strength. Qualitative conformance with the expectations of the simple kink formation analysis described in Appendices I and II is thus apparent (a more quantitative interpretation is not warranted at this stage). These results indicate that further improvements in kink resistance should accompany a reduction in the size of the larger intrabundle inhomogeneities (i.e., void regions and regions of initial curvature) and an enhancement of the matrix yield strength (e.g.,



reduction in porosity, substitution or addition of high strength matrix constituents).

3.4.2 Penetration Tests

The penetration damage involves additional considerations. The kinks in the axial longitudinal bundles have both in-plane and out-of-plane characteristics: the in-plane kinks usually occur as pairs of opposite sign, allowing the lateral displacement of the bundle to remain invariant. The kink locations within the bundle do not relate to the out-of-plane orthogonal bundles, indicating that there is little damage enhancement associated with these features. The zone directly beneath the crater is intensely kinked; the kinks within the zone do not appear to initiate at obvious inhomogeneities. However, toward the limit of penetration of the kink damage, the kinks are almost invariably associated with pre-existent bundle inhomogeneities (especially voids and/or bundle curvature). These kink characteristics are consistent with the damage anticipated for axial compressive deformation of a bundle, as noted above. The remote kinks occur in regions of relatively low deformation (Appendix III) and must seek a severe inhomogeneity to satisfy the kink formation requirements; while the kinks close to the projectile interface develop in regions of much larger stress, and can thus initiate at more abundant small inhomogeneities.

The interrelation between the extent of kinking, \hat{z} , the penetration pressure and the kink formation probability can be found directly from Eqs. (2), (5), and (A30). If it is assumed that the remote kinks are influenced by the remote elastic stress field (Eq. A30b), the probability $\hat{\phi}$



that kink initiation will occur in an axial bundle, outside a zone of depth \hat{z} , is

$$-\ln [1 - \hat{\Phi}] = A_b \lambda_b \int_0^{\infty} \int_0^{\beta^* p_0 (a/z)^2} (S/S^*)^k dS dz \quad (7)$$

Integration and rearrangement then gives;

$$\hat{z} = \left[\frac{\lambda A_b (\beta^* p_0 a^2)^{k+1}}{(S^*)^k (k+1) (2k+1) (-\ln (1-\hat{\Phi}))} \right]^{1/(2k+1)} \quad (8)$$

By choosing a suitably small value for $\hat{\Phi}$ (e.g., 0.01), \hat{z} becomes the extent of the damage zone. It is instructive to obtain ratios of \hat{z} at constant $\hat{\Phi}$ for the three materials with comparable bundle dimension (A,B,C), by inserting the measured kink formation parameters (Fig. 7) and the penetration pressures (Table III) into Eq. (8). The resultant ratios, referred to material C, are indicated in Table III. The correlation with the measured values (obtained at low penetration rates) is quite good, indicating the self-consistency of the measurement techniques.

The damage in the lateral bundles derives from both the non-axial deflection and the axial deformation (e.g., Eq. A42). The deflection stresses increase as the projectile interface is approached (x decreases). Yet, the only kinking that occurs beneath the penetration zone ($x \sim 0$) is the complex kinking associated with the compression between orthogonal lateral bundles (Fig. 9). Also, fractures are occasionally observed in this zone (Fig. 9). The quasi-static deformation field (Fig. 23) indicates axial tension in this



region; implying that kink formation is suppressed by axial tension. Presumably, the tension tends to reduce the severity of pre-existent inhomogeneities (reduces \hat{y} in Eq. A19) and prevents kink instability conditions from being attained, even though the non-axial bundle deflections are relatively large. In principle, the incidence of fracture in the various materials could be ascertained by equating the bundle stresses in the tensile zone (e.g., Eq. A18) to the fiber fracture probability. Fracture data are not presently available for each material, and the comparison cannot, therefore, be conducted at this juncture.

The kinking that occurs in the zone of axial compression ($x/z \gtrsim 1/\sqrt{2}$) tends to concentrate at orthogonal lateral bundles (Fig. 9). The local deflections at these bundles must, therefore, exert an important influence on kink initiation. This can be qualitatively rationalized by noting that the curvature due to the local deflection (Eq. A40) decreases less rapidly with distance x from the penetration axis than the curvature due to the general deflection (Eq. A35); indicating that the former should dominate at appreciable values of x . The role of the axial compression is to preserve, and perhaps accentuate, the influence of local inhomogeneities on the formation of a kink instability. Assuming that axial compression only preserves the inhomogeneities, inserting the measured kink initiation stresses (Fig. 5), penetration pressures (Table III) and projectile radii (500 μm) into Eq. A42, the lateral extent x of kinking in each material can be estimated ($E_f/\langle E \rangle$ is taken to be 10^2 , Table II). The analysis indeed confirms that the local deflection term is dominant, and predicts values of $\hat{x} \approx 2$ mm, reasonably consistent with the present observations (Fig. 9).



The kinking in the non-axial longitudinal bundles is expected to differ from that in the lateral bundles because there is no axial tension near the surface to restrict the formation of kinks at locations of maximum curvature ($z \sim 0$). Intense kinking can thus be anticipated near the surface, in accord with the observations (Fig. 8).

4.0 IMPACT TESTS

4.1 TEST TECHNIQUES

The method of particle impact testing is an exploding foil apparatus⁽⁹⁾ that permits small spherical projectiles to be propelled toward a target at very high velocities (up to $\sim 7,000 \text{ ms}^{-1}$) with excellent accuracy. This apparatus was used to propel 1 mm diameter glass spheres onto carbon composite targets of the type listed in Table I. The targets were typically cylindrical in shape, 2.5 cm in diameter and ~ 3 cm thick.

After testing, damage overviews were obtained in the scanning electron microscope. Then, the targets were vacuum impregnated with polymer, and sections through the crater suitable for subsequent optical microscopy, were prepared by polishing with slurries of fine alumina powders. The subsurface damage on successive sections was then pictorially recorded, using partially polarized light microscopy.

4.2 DAMAGE CHARACTERIZATION

The damage in all cases consisted of a zone of material removal (the crater), bundle kinks and occasionally, bundle fractures. Typical craters



(Fig. 10) consist⁽¹⁾ of a central deep penetration zone and a shallower outer ledge. The dimensions of the crater vary systematically with the impact velocity (Fig. 10). There is also a significant dependence on the bundle dimensions⁽¹⁾ but no discernable effect of the fiber/matrix properties.

The kink damage surrounding the crater exhibits the general features depicted in Figs. 1, 11-15. The effects of impact velocity and microstructure on the maximum depth, \hat{z} , of kinking in the longitudinal bundles (Figs. 11-14) are summarized in Fig. 16. The kink depth increases monotonically with velocity, depends prominently on the fiber/matrix properties and marginally on the relative bundle dimensions. An important observation, comparable to that for the penetration test, is that the longitudinal bundle kinks appear to form homogeneously immediately beneath the crater (i.e., their density is high and they completely traverse the bundle); but are almost invariably associated with microscopic inhomogeneities at their maximum depth of penetration (Figs. 14a and b). The inhomogeneities that are most frequently associated with these kinks are: missing fiber segments, severely distorted fibers, major fiber/matrix disbonds, matrix voids. An unusual mode of kinking (Fig. 14a) is also observed occasionally in materials A and B, occurring at the corners of out-of-plane lateral bundles.

The corresponding trends in the maximum lateral extension, \hat{x} , of kinks in the lateral bundles (Fig. 15) are summarized in Fig. 17. The extent of this mode of kinking is very sensitive to the impact velocity and microstructure; substantial effects of velocity, bundle dimensions and fiber/matrix properties are apparent. Complex kinking and fracture of the lateral bundles is also apparent beneath the penetration axis (Fig. 15).



4.3 DAMAGE INTERPRETATION

The strong effects of velocity on the relative extent of kinking in both the axial longitudinal and lateral bundles indicates that these key modes of damage cannot be interpreted by a simple extension of the quasi-static analysis described previously (Section 3.4). A fully dynamic analysis is required. The complexity of the dynamic problem requires that numerical techniques be developed for detailed damage analysis and interpretation. An approach is described in the following section (Section 5).

A qualitative interpretation of the damage in terms of available (isotropic) dynamic solutions can, however, provide some useful insights. The ratios of the damage depths \hat{z} in the axial longitudinal bundles, for materials A and B versus material C, are greater at high impact velocities than the equivalent quasi-static values (Fig. 16). The most self-consistent interpretation of this observation is that the spatial dependence of the dynamic stress is less than the quasi-static dependence, providing a greater dependence of the damage depth on the kink formation stress (see Section 3.4). Such behavior is anticipated by the solutions for a pressurized cavity.^(10,11) (Also, the high modulus fibers could lead to a partial wave-guide phenomenon, further reducing the geometric attenuation typically attributed to spherical waves.) Specifically, if it is assumed that the ratio of dynamic penetration pressures is similar throughout to the values obtained in the penetration tests (Table III), a generalized form of Eq. (8)

$$\hat{z} = \left[\frac{\lambda A_b (\beta^* p_0 a^n)^{k+1}}{(S^*)^k (k+1) [n(k+1) - 1] [-\ln(1-\hat{\phi})]} \right]^{1/[n(k+1) - 1]} \quad (9)$$



SC5076.5FR

where n is the spatial exponent of the stress field ($\sigma_z \propto (a/z)^n$), indicates that the observed \hat{z} ratios at high velocities ($\geq 4,000 \text{ ms}^{-1}$) are consistent with a linearly decreasing stress field (i.e., $\sigma_z \propto 1/z$). The alternative, but less plausible, interpretation of the dynamic influence would require that the relative dynamic penetration pressures be substantially different from those obtained quasi-statically.

The even stronger velocity dependence of kinking in the lateral bundles (Fig. 17) suggests that additional dynamic phenomena are involved. Available dynamic solutions indicate that the dynamic stress field for a rigid projectile and a plastically deforming target are relatively uniform about the center of impact.⁽¹¹⁾ The tendency for kinking in the lateral bundles to be comparable to that in the axial longitudinal bundles might, therefore, be anticipated. The observed greater extent of the lateral bundle kinking is thus, presumably, associated with the non-axial displacement of the lateral bundles, coupled with the dynamic axial compression. The observed in-plane morphology of the kinks in the lateral bundles⁽³⁾ (Fig. 15) is consistent with this interpretation.

Finally, the consistent trends in the effect of microstructure on the three measured properties--the extent of the kink zone, the yield strength in constrained compression, and the penetration pressure--is re-emphasized. Further study is, of course, needed to establish the quantitative interdependence of these properties (i.e., a dynamic equivalent of Eq. 8); but, meanwhile, these relatively simple quasi-static tests should provide a measure of a material's kink resistance, suitable for inclusion in materials development studies.



5.0 NUMERICAL CALCULATION OF KINKING

A preliminary attempt at the numerical calculation of kinking in the longitudinal bundles has been undertaken using an Eulerian finite difference method (the HELP code).⁽¹²⁾ The calculation was conducted using the axisymmetric configuration shown in Fig. 18; in which a 500 μm radius glass sphere was directed to impact the axis of a cylindrical rod, having the average properties of a fiber bundle (Table II). The surrounding material was taken to be isotropic, having the average properties of both the graphite matrix and the fiber bundles (see Table II).

5.1 COMPUTATIONAL SCHEME

The computational grid was chosen to have the finest resolution (Fig. 18b) adjacent to the bundle axis, and at a depth where experiment (Fig. 16) had indicated that kink damage could be anticipated. The equation of state used to describe the material response was:

$$p = A\xi + B\xi^2 \quad (10)$$

where p is the hydrostatic pressure, A and B are the constants listed in Table IV; ξ is the volumetric strain, which is related to the density change by:

$$\xi = \rho/\rho_0 - 1 \quad (11)$$

where ρ_0 is the initial density. The anisotropic constitutive model applied to the bundle has been documented elsewhere.⁽¹²⁾ The glass and matrix



SC5076.5FR

materials were modeled, respectively, as isotropic, linear strain hardening and elastic/perfectly plastic. In both cases, a von Mises yield criterion was assumed,

$$S_{ij}S_{ij} \leq \sigma_y^2 \quad (12)$$

where S_{ij} is the stress deviator tensor and σ_y is the plastic flow stress in shear given by;

$$\sigma_y = (\sigma_y^0 + \sigma_y' \xi) (1 - U/U_m) \quad (13)$$

σ_y^0 is the yield stress at zero pressure, σ_y' is a measure of the pressure dependence of the yield stress; U , the specific internal energy, and U_m , the energy at melting, are introduced to provide an approximate measure of the temperature dependence of the yield stress. The values of the yield parameters chosen for the calculation are summarized in Table IV. The values for glass were obtained from shock wave compression tests⁽¹³⁾ and probably represent compressive fracture rather than plastic yield. The matrix yield strength was obtained from the values measured for material C (Table II); the bundle yield strengths were taken to be the same as the matrix in the transverse direction, but appreciably larger in the axial direction (large enough that kinking always preceded macroscopic plastic yield, in accord with observations).

Kinking of the bundle was considered to initiate (Section 3.4) whenever the stress differential in the bundle, $\sigma_{zz} - \sigma_{rr}$, exceeded a critical value of 400 MPa (Fig. 5). It is recognized that, for statistical



SC5076.5FR

reasons, this is likely to be an underestimate of the kink initiation stress pertinent to the impact of a single bundle (i.e., an overestimate of the kink zone size). However, it is a representative value suitable for present purposes. Kink propagation was assumed to occur relatively slowly (because it involves substantial plastic accommodation of the fractured fiber segments by the matrix⁽³⁾); hence, kink initiation was not considered to produce a significant change in the state of stress within a kinked element during the penetration phase of the impact.

A fracture condition was also invoked to ensure that the tensile stress did not attain unacceptably large values. A maximum tensile stress $\hat{\sigma}$ was attributed to each element, as indicated in Table IV. The element was considered to fracture when the average tensile pressure exceeded $\hat{\sigma}$. This is considered satisfactory for the present problem since discrete crack propagation processes are not involved.⁽¹¹⁾ When the critical tensile stress in an element has been exceeded, the stress deviations and pressures are set to zero. Thereafter, the cell can still support compressive stress. The values of $\hat{\sigma}$ selected for each constituent were best possible values from fracture data in the literature. The limitations of such a selection are recognized, but since fracture is of secondary significance in the present calculation, the choice of $\hat{\sigma}$ is not critical to the final prediction of the kink depth.

A final feature of the calculation was the introduction of an artificial viscosity,⁽¹⁴⁾ which was required to maintain numerical stability in regions of high local strain rate. This introduces an error into the stress calculation. The magnitude of the error is most significant in the



vicinity of the shock front. The error appears to be small, as discussed in detail elsewhere;⁽¹⁴⁾ but clearly, the influence of this viscosity term must be carefully evaluated in each case.

5.2 RESULTS

The contact stress during penetration is plotted in Fig. 19. The value approached toward the final penetration stage (~ 400 MPa) is reasonably close to the measured penetration pressures for material C (Table III), providing some credence to the material properties selected for the calculation. Typical values of the axial and transverse stresses for the center cell at fixed locations along the bundle are plotted in Fig. 20. The oscillation in the stress is considered to derive from transverse inertia effects, typically encountered for Pochhammer-Chree waves propagating in cylindrical bars.⁽¹⁵⁾ The development of the kinks during penetration is indicated on Fig. 21. The calls in which the kink initiation stress has been exceeded are indicated by a horizontal line. Inspection of the figure indicates that an appreciable zone develops toward the final penetration stage in which only the outer two cells of the bundle experience the kink formation stress. These cells experience the requisite stress for a very short duration. It is unlikely that the duration is large enough in most instances to activate fiber fracture (cf. the incubation time for crack activation⁽¹¹⁾). A best estimate of the final kink depth \hat{z} below the crater is thus 4.4 mm (Fig. 21). This is in the same range as the measured values at $6,000 \text{ ms}^{-1}$ (Fig. 16). The results are thus quite encouraging. However, additional insights concerning the incubation time for kink initiation are



clearly needed before fully quantitative damage predictions can be undertaken. Also, a means for incorporating the statistical character of the kink initiation stress must be identified.

6.0 SUMMARY AND IMPLICATIONS

Studies of carbon composites subjected to quasi-static penetration and to projectile impact have demonstrated strong effects of microstructure on the extent of the subsurface damage (manifested as kinks within both longitudinal and lateral bundles). Quasi-static analyses of bundle deformation and the resultant fiber curvature have indicated the important role of pre-existent bundle inhomogeneities (initial fiber curvature, matrix voids) in the kink formation process, axial bundle compression also emerges from the analysis as a prerequisite for kink formation. The analysis permits a self-consistent correlation to be obtained between the measured kink formation stresses, the penetration pressures and the quasi-static extent of the kink damage in longitudinal bundles. It also enables the morphology of the observed kinks and the kink zones to be rationalized.

The kinking that occurs under dynamic conditions can only be qualitatively interpreted using available analyses of the dynamic target deformation. Numerical methods are needed to assist in the development of dynamic damage models. An initial attempt at the numerical computation of kink formation in the longitudinal bundles has thus been instituted with encouraging results. Much additional work is required to develop a working model of impact damage.



The observations, measurements, and analyses of kink formation provide several important implications for the design of damage resistant composites. If the depth of damage in the longitudinal bundles is the damage parameter of primary concern (i.e., the damage in the lateral bundles is of secondary concern), as might be the case for erosion resistance, then the preferred bundle geometry is one that contains the maximum feasible proportion of longitudinal bundles (with a high fiber content): the bundles being disposed on as fine a scale as possible to avert deleterious consequences of the local anisotropy. However, if the extent of damage in the lateral bundles is also of importance, a more uniform array of bundles may be preferred. Additional work is needed to quantify this requirement. In creating the appropriate bundle geometry, it should be ensured that the properties of the microstructural constituents are also optimized. The matrix has a primary role in the kink initiation process. Both analysis and experiment indicate that a matrix with a maximum possible yield strength is generally preferred. Attempts to improve the inelastic properties of the graphite matrix, or to find a substitute material, are thus to be encouraged. However, it should be recognized that there may be an upper limit to the damage resistance that can be imparted by matrix modification, due to either the incidence of another damage mechanism (e.g., matrix fracture) or to an increase in the penetration pressure that more than counteracts the increase in kink resistance. Such eventualities should be appreciated if discouraging results are to be avoided. Another primary kink formation parameter is the distribution of pre-existent bundle inhomogeneities. A reduction in the amplitude of the large extreme of the bundle inhomogeneities should lead to considerable



Rockwell International
Science Center
SC5076.5FR

increases in the kink resistance; and attempts to address this issue should constitute a primary direction for materials development studies.

(Additionally, the fiber fracture strength can exert an influence. It's specific role is presently rather nebulous, because the importance of the fiber strength is contingent on the magnitude of the other constituent properties--particularly the matrix yield strength and the magnitude of the inhomogeneities. Nevertheless, the fiber fracture strength should be included as a property that may correlate with the kink resistance.)

Finally, the consistent trend with microstructure of the extent of the kink zone, the yield stress in constrained compression and the penetration pressure is emphasized. This suggests that these relatively simple quasi-static tests can be used to provide a measure of a material's impact damage resistance, suitable for materials development studies.



APPENDIX I

COMPRESSIVE DISTORTION OF FIBER BUNDLES

The elastic buckling of initially straight laminates has been analyzed by Schuerch⁽¹⁶⁾ and by Rosen⁽¹⁷⁾ using a strain energy method. For the mode of buckling that requires extension of the matrix between the fibers, the critical buckling stress is large, and given by

$$\sigma_c \approx \frac{2V_f^{3/2} \sqrt{E_m E_f}}{3(1-V_f)} \quad (A1)$$

where V_f is the volume fraction of fibers. However, when buckling only subjects the matrix to axial shear, the critical buckling stress is reduced to

$$\sigma_c = \frac{E_m}{2(1+\nu)(1-V_f)} \quad (A2)$$

However, even this stress (~ 8 GPa for a typical bundle, $E_m = 5$ GPa and $V_f \sim 0.8$) is considerably larger than the measured kink initiation stress (0.2-0.5 GPa). The onset of compressive fiber distortion can, therefore, be reasonably supposed to occur in regions of pre-existent curvature at much reduced stress levels.

The deflection of initially curved fibers in a bundle subjected to compressive deformation is resisted by the surrounding matrix. The magnitude of this resistance depends on the presence of interface disbonds and matrix voids, as well as the compressibility, shear modulus, and shear strength of the matrix. Consider the fairly typical case, depicted in Fig. 22, of a



SC5076.5FR

matrix void coincident with the plane of fiber curvature. The deflection of the adjacent fiber is then dictated by the applied force P and the resistance imparted by the material on one side of the fiber. This resistance is initially supplied by the elastic stiffness of the matrix, as augmented by the flexural stiffness of the nearest neighbor fibers. The subsequent, inelastic resistance is related to the compressibility and shear strength of the matrix. Assuming that inelastic matrix deformation dominates at the relatively large fiber distortions pertinent to kink formation, the fiber behavior can be analyzed by examining the solution for an initially curved elastic beam subjected to end forces P and supported along its length by a uniform stress q (Fig. 22). Let the initial curvature y_0 be represented by (18)

$$y_0 = \hat{y} \sin \pi(x/l) \quad (A3)$$

where the dimensions x , l , and \hat{y} are shown on Fig. 22. When the load P is applied, the deflection y is related to the bending moment M by;

$$M = Py - \frac{qlxb}{2} + \frac{qx^2b}{2} \quad (A4)$$

where b is the beam width. The bending moment is also related to the deflection y' due to the deformation by;

$$M = -EI \left(\frac{d^2y'}{dx^2} \right) \quad (A5)$$

where, $y' = y - y_0$. Combining Eqs. (A3), (A4), and (A5) gives



$$EI \frac{d^2 y'}{dx^2} + \frac{qx^2 b}{2} - \frac{qlxb}{2} + Py' + P\hat{y} \sin \pi(x/l) = 0 \quad (A6)$$

Differentiating Eq. (A6) twice with respect to x then gives

$$\left(\frac{EI}{P}\right) \frac{d^4 y'}{dx^4} + \frac{qb}{P} + \frac{d^2 y'}{dx^2} - \hat{y} \left(\frac{\pi}{l}\right)^2 \sin \left(\frac{\pi x}{l}\right) = 0 \quad (A7)$$

This differential equation has a general solution of the form

$$y' = A \sin kx + B \cos kx + Cx + D + F \sin(\pi x/l) - qbx^2/2P, \quad (A8)$$

where $k^2 = P/EI$ and A, B, C, D, F are constants of integration. Applying the boundary conditions

$$y' = d^2 y' / dx^2 = 0$$

at $x = 0$ and $x = l$, we obtain;

$$-B = D = qb/k^2 P$$

$$A = (qb/k^2 P) [(\cos(kl) - 1) / \sin(kl)]$$

$$C = ql/2P$$

$$F = \hat{y} k^2 / (\pi/l)^2 - k^2$$

The final equation for the deflection is thus;

$$y = \frac{\hat{y} (\pi/l)^2}{[(\pi/l)^2 - k^2]} \sin(\pi x/l) - \frac{qb}{Pk^2} \left[\frac{[1 - \cos(kl)]}{\sin(kl)} \sin(kx) + \cos(kx) - \frac{k^2 x l}{2} - 1 + \frac{x^2 k^2}{2} \right] \quad (A9)$$

The first term is due to the initial curvature of the beam and the second term is due to the matrix resistance. In applying this expression, it should be



recalled that it relates only to the deflection that occurs when the matrix resistance is inelastic: it cannot be used to predict the initial beam deflections (which elicit an elastic matrix response).

The fiber curvature, κ , the inverse of the radius of curvature can now be derived from Eq. (A9), as,

$$\kappa = \frac{-\hat{y}(\pi/l)^4}{[(\pi/l)^2 - k^2]} \sin(\pi x/l) - \frac{qb}{P} \left[1 - \cos(kx) - \frac{[1 - \cos(kl)]}{\sin(kl)} \sin(kx) \right] \quad (A10)$$

This has a maximum negative value at $x = l/2$ given by,

$$\hat{\kappa} = \frac{-\hat{y}(\pi/l)^4}{[(\pi/l)^2 - k^2]} + \frac{qb}{P} \left[\frac{1 - \cos(kl/2)}{\cos(kl/2)} \right] \quad (A11)$$

The stress q that restricts the development of curvature in initially distorted fibers transmits lateral forces to the adjacent, initially straight fibers (Fig. 22). This induces premature buckling of the straight fibers, and propagates the zone of fiber curvature. The displacement of the force P needed to develop the curvature anticipated by Eq. (A10) is not, therefore, restricted by the high compressive stiffness of the surrounding initially straight fibers. We thus propose to use Eq. (A10) as a direct measure of the relation between the fiber curvature, the applied stress, and the matrix resistance. The applied stress p is introduced by assuming that the stiffness of the fibers still greatly exceeds the matrix stiffness; then, for a fiber of square cross section⁽¹⁾

$$P \approx pb^2/A_f \quad (A12)$$



where A_f is the area fraction of fibers within a bundle. Noting that the moment of inertia is $b^4/12$, the maximum curvature becomes,

$$\hat{\kappa} = \frac{\pi^4 \hat{y}}{[1^2 \pi^2 - 12V_f(p/E_f)(1/b)^2/A_f]} + \frac{(q/p)A_f}{b} \frac{1 - \cos \left[(1/b) \sqrt{3V_f(p/E_f)/A_f} \right]}{\cos \left[(1/b) \sqrt{3V_f(p/E_f)} \right]} \quad (A13)$$

Expanding the cosine terms,

$$\cos x = 1 - x^2/2 + x^4/24 - \dots$$

we note that for small $(1/b)^2(p/E_f)/A_f$,

$$\hat{\kappa} = - \frac{\pi^4 \hat{y}^2}{[\pi^2 - 12(p/E_f)(1/b)^2/A_f]} + \frac{3(q/E_f)(1/b)^2}{2b [1 - 3(1/b)^2(p/E_f)/2A_f]} \quad (A14)$$

Rearranging, enables the critical applied pressure p_c for fiber fracture or kinking to be approximately expressed as,

$$p_c \approx \frac{2}{3} \left(\frac{b}{l} \right)^2 E_f A_f \left[1 - \frac{1}{\hat{\kappa}_c} \left(\frac{\pi^4 \hat{y}}{1^2} - \frac{1.51^2 q}{b^3 E_f} \right) \right] \quad (A15)$$

where $\hat{\kappa}_c$ is the critical (negative) local curvature required to induce fiber fracture or kinking. For small matrix shear strengths ($q \ll E_f$), the initial dimensions of the inhomogeneity (\hat{y}, l) become the dominant parameters, yielding,

$$p_c \approx \frac{2}{3} E_f A_f \frac{b^2}{l^4} \left[1^2 - \frac{\pi^4 \hat{y}}{\hat{\kappa}_c} \right] \quad (A16)$$



SC5076.5FR

indicating that p_c decreases as the dimensions of the inhomogeneity increase. Relating $\hat{\kappa}_c$ to a nominal fiber fracture stress, σ_f , through;

$$\sigma = E_f b \left| \hat{\kappa}_c \right| / 2 \quad (A17)$$

the critical applied stress for fiber fracture becomes,

$$p_c^f \approx \frac{2}{3} A_f E_f \frac{b^2}{l^4} \left[l^2 - \frac{\pi^4 \hat{y} b}{2} \left(\frac{E_f}{\sigma_f} \right) \right] \quad (A18)$$

indicating that fracture is impeded by a large fiber fraction and fiber fracture stress; but could be either adversely or beneficially influenced by a large modulus or a large fiber radius, depending on the relative magnitude of the other variables.

Alternatively, relating $\hat{\kappa}_c$ to a kink formation stress (Appendix II, Eq. A22), the critical uniaxial compressive stress for kinking becomes,

$$p_c^k \approx \frac{2}{3} A_f E_f \frac{b^2}{l^4} \left[l^2 - \frac{\pi^5 \hat{y} b}{2 \sigma_m} \sqrt{\frac{6 E_f \mu_m}{V_f (1 - V_f)}} \right] \quad (A19)$$

In this instance, a large matrix yield strength σ_m replaces the fiber fracture strength as a dominant parameter: while the other parameters (\hat{y} , l , b , E_f) occupy similar roles.



APPENDIX II
KINK INITIATION

The initiation of a kink is expected to ensue whenever a series of correlated fiber fractures, that satisfy the condition for mechanical instability, are developed;⁽³⁾ usually, this will not be coincident with the first fiber fracture.⁽³⁾ Consequently, the mechanics of kink formation are intricate, and are too complex to attempt to derive definitive relations at this juncture. Some important insights can be gained, however, by examining the fracture of laminates consisting of a brittle elastic and a ductile constituent.⁽¹⁹⁾ For fiber fracture represented by the relation

$$\Phi(S) = 1 - \exp \left[- \int_A (S/S_0)^m dA \right] \quad (A20)$$

where m , and S_0 are distribution parameters (cf. Eq. (2)) and A is the surface area of stressed fiber, the critical tensile stress σ^c at instability is given by the relation,^(3,19)

$$\left(\sigma_\infty^c\right)^{m-3} = \frac{2 S_0^m}{(3\pi m b w \sigma_m^3) \ln \left[(3\pi^2 \mu_m / E_f V_f (1-V_f)) \left(\sigma_\infty^c / \sigma_m\right)^2 \right]} \quad (A21)$$

where w is the width of the bundle. This is a complex relation in σ_∞^c , and insights into the factors that influence σ_∞^c can only be obtained for specific situations. An important case is, $\mu_m \ll E_f$ and $m < 10$. For



example, when $m = 5$ (an experimental value for material C is $8^{(3)}$),
expanding the logarithmic term in Eq. (A21) gives

$$\sigma_{\infty}^C \approx \frac{\sigma_m}{\pi} \sqrt{\frac{E_f V_f (1 - V_f)}{6 \mu_m}} \quad (A22)$$

In this case the fiber fracture parameters (S_0, λ) are relatively unimportant: the matrix yield strength is the dominant influence. In other situations, however, the fiber fracture parameters can exert a more important influence.



APPENDIX III
PROJECTILE PENETRATION

The intrafiber stresses that derive from an imposed fiber curvature are dictated primarily by the elastic properties of the high stiffness fibers. The role of the matrix is to maintain a separation between fibers, by virtue of their resistance to shear and compression; it has little effect on the stresses within the fibers (i.e., a maximum axial shear stress given by the matrix shear strength, τ_m). However, the bundle displacements and fiber curvatures that occur in response to an imposed force can be strongly influenced by the properties of the matrix. These properties of the composite suggest the following method for evaluating the incidence of fiber fracture and kinking. The approximate displacements of the bundles are first determined from relations derived for isotropic elastic or elastic/plastic media (most pertinent to three-dimensional composites); allowing the fiber curvatures that develop in response to the bundle displacement to be obtained. Then the tensile stresses within the fibers are deduced from the fiber curvatures and equated to the fiber fracture stress or the kink initiation stress.

1.0 BUNDLE DISPLACEMENT

The medium response during the quasi-static elastic/plastic penetration of a half space by a rigid sphere has been shown to conform quite closely to two relatively simple limit solutions.⁽²⁰⁾ The elastic/plastic



solution for a pressurized spherical cavity provides a reasonable description close to the projectile interface; while, the response in the elastic zone remote from the interface is most effectively described by the elastic (Hertzian and Bousinesq) solution for a half space. The response at intermediate locations can be estimated by interpolation. The radial displacement within the elastic zone close to the projectile, predicted by the spherical cavity solution,⁽²¹⁾ is,

$$u_r = \frac{\sigma_y r_p^3 (1 + \nu)}{3 \langle E \rangle r^2} \quad (r > r_p) \quad (A23)$$

where ν is Poisson's ratio, $\langle E \rangle$ is the average Young's modulus of the composite, r_p is the radius of the plastic zone, σ_y is the yield strength and r is the distance from the center of the cavity. The plastic quantities r_p and σ_y are related to the conditions that exist within the zone of intense fiber/matrix distortion near the projectile interface, Fig. 9. However, we note that r_p for large plastic deformations rapidly attains a limiting value, related to the current cavity radius r_j , by,⁽²¹⁾

$$(r_p/r_j)^3 = \langle E \rangle / 3\sigma_y (1 - \nu) \quad (A24)$$

Substituting this relation for r_p into Eq. (A23), the radial displacement becomes,

$$(u_r/r) = \frac{1}{q} (1 + \nu)/(1 - \nu) (r_j/r)^3 \quad (A25)$$



SC5076.5FR

The displacements thus depend on the cavity radius, but do not exhibit a specific dependence on the plastic properties of the material.* The analogous large deformation result for the plastic zone is:⁽¹⁰⁾

$$u_r/r = 1 - \left\{ [1 - (r_j/r)^3] [1 - 2(1 - 2\nu)(\sigma_y/\langle E \rangle)]^{-1} \right\}^{1/3} \quad (\text{A26})$$

For the typical condition, $\sigma_y < \langle E \rangle$, Eq. (A26) reduces to:

$$u_r/r = 1 - [1 - (r_j/r)^3]^{1/3} \quad (\text{A27})$$

Again, therefore, there is no specific dependence on the plastic properties of the material. The displacements close to the projectile interface thus assume a particularly simple form (Fig. 23).

The elastic displacements remote from the projectile interface--given by the half space solution--are not radially symmetric, but have a horizontal component u_x and a vertical component u_z given by:⁽²²⁾

$$u_x = \frac{(1 - 2\nu)(1 + \nu)p_0 a^2}{2 \langle E \rangle x} \left[z(x^2 + z^2)^{-1/2} - 1 + x^2 z (x^2 + z^2)^{-3/2} (1 - 2\nu)^{-1} \right]$$

$$u_z = \frac{p_0 a^2}{2 \langle E \rangle} \left[(1 + \nu) z^2 (x^2 + z^2)^{-3/2} + 2(1 - \nu^2)(x^2 + z^2)^{-1/2} \right] \quad (\text{A28})$$

*This result applies strictly to incompressible plasticity. The equivalent result for compressible deformation, as might pertain in porous materials, has not been derived.



where p_0 is the contact pressure and a is the contact radius. The remote displacements thus exhibit direct dependencies on the plastic properties, through p_0 , and on the projectile radius, through a . The displacement characteristics along the surface and along the penetration axis, predicted by these limit solutions, are schematically indicated in Fig. 23. Note that there is a region of zero displacement along the surface, because the cavity and half space solution predict displacements u_x of opposite sign.

2.0 FIBER FRACTURE AND KINKING

The general curvature of fibers within bundles can be derived directly from the above displacement relations. Local curvatures (e.g., around orthogonal bundles at inhomogeneities) are superimposed on the general curvatures. The important trends are encompassed by examining longitudinal bundles along the penetration axis, lateral bundles just beneath the surface and longitudinal bundles beside the penetration axis.

2.1 AXIAL LONGITUDINAL BUNDLES

The longitudinal bundles along the penetration axis are subjected to axial compression; there is no general curvature. However, a local curvature associated with microstructural inhomogeneities (or elastic buckling) can occur, as a direct consequence of the compressive deformation (Appendix I). This curvature is related to the magnitude of the deformation, the matrix shear strength, the fiber modulus and volume fraction, and the dimensions of



the inhomogeneity. The elastic deformation is given in the vicinity of the projectile interface by:

$$\xi_z = - \left\{ 2/9(1 - \nu) \right\} (r_j/z)^3 \quad (\text{A29c})$$

and in remote regions by:

$$\xi_z = - 3p_0 a^2 / 2 < E > z^2 \quad (\text{A29b})$$

The equivalent stresses within the longitudinal bundles are,

$$p_z = - E_b \left[2/9(1 - \nu) \right] (r_j/z)^3 = \beta (r_j/z)^3 \quad (\text{A30a})$$

$$p_z = - 3 (E_b / < E >) p_0 a^2 / 2 z^2 = \beta^* p_0 (a/z)^2 \quad (\text{A30b})$$

These relations should permit the measured kink stresses (Section 3.2) and penetration pressures (Section 3.3) to be correlated with the depth of damage in the axial longitudinal bundles (Section 3.3). More fundamental predictions of kinking and the relation to microstructure involve a combination of Eq. (A30) with fiber fracture relations or kink formation relations.

2.2 LATERAL BUNDLES

The lateral bundles are subjected to a general curvature related to the displacement u_z . Near the projectile interface, the curvature K in the elastic zone can be obtained from Eq. (A23) as:

$$K = \frac{\partial^2 u_z}{\partial x^2} = 3 \frac{r_j^3 z (4x^2 - z^2) (1 + \nu)}{(x^2 + z^2)^{3/2} (1 - \nu)} \quad (\text{A31})$$



The curvature has a minimum (Fig. 24) at $x = 0$ given by:

$$\kappa_{\min} = -3 (1 + \nu) r_j^3 / z^4 (1 - \nu) \quad (A32)$$

and maxima at $x = \pm 3/4 z$, given by:

$$\kappa_{\max} = 0.85 (1 + \nu) r_j^3 / z^4 (1 - \nu) \quad (A33)$$

The curvature in the plastic zone, derived from Eq. (A27), has similar characteristics. In the elastic zone, remote from the projectile, the curvature derived from Eq. (A28) is,

$$\kappa = \frac{-2p_0 a^2 (1 + \nu)}{\langle E \rangle (x^2 + z^2)^{3/2}} \left[8x^4 + 3x^2 z^2 + \nu (2x^4 - 9x^2 z^2 - z^4) \right] \quad (A34)$$

which, near the surface ($z \ll x$) becomes:

$$\kappa = \frac{4p_0 a^2 (1 + \nu)}{\langle E \rangle x^3} (4 + \nu) \quad (A35)$$

Additional local curvature of the lateral bundles can occur in regions where the deflection u_z exceeds the elastic limit of the matrix interstice. The orthogonal lateral bundles then exhibit a greater resistance to distortion than the adjacent interstices, and perturb the deflection of the bundle^(1,3). The local curvature is derived from the equation for the local deflection, as a function of distance x' from the local support⁽²²⁾

$$(u_z)_l = \frac{\delta}{2} \left(\frac{x'}{l} \right) \left[12 \left(\frac{x'}{l} \right) - 9 - 4 \left(\frac{x'}{l} \right)^2 \right] \quad (A36)$$



and is given by,

$$\kappa_l = \frac{12}{l^2} \left[1 - \frac{x'}{l} \right] \quad (\text{A37})$$

where δ is the relative displacement of adjacent out-of-plane lateral bundles and l is the spacing between bundles. The maximum curvature, at $x' = 0$ is,

$$\kappa_l = \frac{12\delta}{l^2} \quad (\text{A38})$$

The local displacement δ is, at most, equal to the differential in the general displacement u_z at two locations x and $x + l$ along the bundle. For example, the relative displacement of near surface lateral bundles (small z) remote from the projectile is (from Eq. A28)

$$\delta \leq l p_0 a^2 (1 - \nu^2) / \langle E \rangle x (x + l) \quad (\text{A39})$$

giving,

$$\hat{\kappa}_l \leq 12 p_0 a^2 (1 - \nu^2) / \langle E \rangle x (x + l) l \quad (\text{A40})$$

The lateral bundles are also subjected to tensile and compressive deformations. In the elastic zone near the projectile (Eq. A25),

$$\epsilon_x = \frac{r_j^3}{9(1-\nu)} \left[\frac{(z^2 - 2x^2)}{(x^2 + z^2)^{5/2}} \right] \quad (\text{A41})$$

The deformations are thus positive (tensile) for $x/z \leq 1/\sqrt{2}$ and negative (compressive) for $x/z \geq 1/\sqrt{2}$ (Fig. 24). The tensile deformation of an



initially straight fiber does not produce fiber curvature; whereas, the tensile deformation of an initially curved fiber tends to straighten the fiber and eliminate the curvature. Conversely, compressive deformation, as noted above, tends to generate curvature at local inhomogeneities.

The stresses that derive from the general flexural curvature, the local curvature and the axial deformation can be added to obtain the total stress, σ_{xx} . In the tensile zone, σ_{xx} can be equated to the fracture stress to estimate the incidence of fracture. In the compressive zone, it must be recognized that the compressive deformation is augmented at local inhomogeneities (Appendix I), requiring that the axial term be coupled with Eq. (A22) before the onset of kinking can be predicted by equating σ_{xx} to the kink initiation stress.

2.3 NON-AXIAL LONGITUDINAL BUNDLES

The longitudinal bundles beside the crater are subject to curvature associated with the displacement u_x . However, near surface relaxations limit the development of a general curvature in the immediate subsurface, as well as restricting the zone of tensile deformation. Otherwise, the fiber curvatures are similar to those anticipated for the lateral bundles.



REFERENCES

1. W. F. Adler and A. G. Evans, in Erosion: Prevention and Useful Applications, ASTM Special Technical Publication (W. F. Alder, editor), in press
2. L. Rubin, Impact Damage Mechanisms of 3-D Carbon-Carbon Material, Space and Missile Systems Organization, TR-76-142 (July 1976)
3. A. G. Evans and W. F. Adler, Acta Met. 26 (1978), 725
4. A. G. Evans, Jnl. Composite Materials, to be published
5. C. R. Chaplin, Jnl. Mater. Sci., 12 (1977), 347
6. C. W. Weaver and J. G. Williams, Jnl. Mater. Sci., 10 (1975), 1323
7. J. W. Matthews, F. A. McClintock, and R. A. Shack, Jnl. Amer. Ceram. Soc., 59 (1976), 304
8. J. C. Aleszka, M. A. Ferdman, and W. F. Adler, Effects Technology Report CR77-402 (September 1977)
9. J. D. Carlyle, M. E. Graham, and T. L. Menna, Review of Scientific Instruments, 46 (1975), 1221
10. H. G. Hopkins, Progress in Solid Mechanics Vol. 1 (Ed. I. N. Sneddon and R. Hill), Interscience, New York (1960), p. 85
11. A. G. Evans, Treatise on Materials Science and Technology, New York: Academic Press, in press
12. G. A. Gurtman, L. J. Hageman, J. K. Dienes, and M. H. Rice, Hypervelocity Impact of Three-Dimensionally Reinforced Carbon/Carbon Composites, SAMSO TR-77-J-12 (June 1976)
13. J. Wackerle, J. Appl. Phys. 33 (1962), 922
14. L. J. Hageman, D. E. Wilkens, R. T. Sedgwick, and J. L. Waddell, "HELP, An Eulerian Program in Two Space Dimension," SSS-R-75-2656 (July 1975)
15. R. Folk, G. Fox, C. A. Shook, C. W. Curtis, Jnl. Acoustic Soc. Amer., 30 (1958), 552
16. H. Schuerch, AIAA Journal, 4 (1966)
17. B. W. Rosen, Mechanics of Composite Strengthening, ASM Seminar, Philadelphia, Pennsylvania (October 1964)



SC5076.5FR

18. S. Timoshenko and J. M. Gere, Theory of Elastic Stability (McGraw-Hill, New York) 1961
19. A. S. Argon, Treatise on Materials Science and Technology New York: Academic Press, 1972, Vol. 1, p. 79
20. A. G. Evans, "The Fracture Toughness of Ceramics: The Role of Indentation Techniques," ASTM Special Technical Publication, in press
21. R. Hill, The Mathematical Theory of Plasticity (Clarendon Press, Oxford) 1956
22. S. Timoshenko and J. N. Goodier, Theory of Elasticity (McGraw-Hill, New York) 1951

TECHNICAL REPORTS

- A. G. Evans, J. C. Chesnutt and W. F. Adler, Impact Damage in Carbon/Carbon Composites, Progress report for period 05/01/76 thru 10/31/76 - SC5076.1MR
- A. G. Evans, Impact Damage in Carbon Composites, End of Year Report, 12/01/76
- A. G. Evans, W. F. Adler and J. C. Chesnutt, Impact Damage in Carbon/Carbon Composites, Technical Report for period 05/01/76 thru 12/31/76 - SC5076.2TR
- A. G. Evans and W. F. Adler, Structural Degradation in Fiber Composites by Kinking, Technical Report for period 05/01/76 thru 04/30/77 - SC5076.3TR
- W. F. Adler and A. G. Evans, Impact Damage in Carbon-Carbon Composites, Technical Report for period 05/01/77 thru 10/31/77 - SC5076.4TR
- A. G. Evans, Impact Damage in Carbon Composites, End of Year Report, 12/01/77



TABLE I
PROPERTIES OF MATERIALS SELECTED FOR PRESENT STUDY

Material	Reinforcing Fibers	Processing Sequence	Unit Cell Dimensions (mm)			Relative Bundle Areas		
			x	y	z	x	y	z
A	Pitch VS0022	CVD/A240	0.76	0.76	1.14	1	1	1
B	Pitch VS0022	CVD/LS24	0.76	0.76	1.14	1	1	1
C	Thorne1 50	CVD/Pitch	0.76	0.76	0.84	2	2	3
D	Thorne1 50	CVD/Pitch	0.76	0.76	0.76	1	1	5
E	Thorne1 75	Pitch/CVD/Pitch	1.02	1.02	0.56	1	1	13



TABLE II
APPROXIMATE ELASTIC AND PLASTIC
PROPERTIES OF THE COMPOSITE CONSTITUENTS

Material	Test Method	Apparent Young's Modulus (GPa)			Apparent Uniaxial Yield Strength of Matrix (MPa)
		Bundle		Matrix	
		Axial	Transverse		
A	In-Situ	220	10	3	18
	Isolated	190	12	4	
B	In-Situ	240	12	3	20
	Isolated	200	10	4	
C	In-Situ	200	8	5	30
	Isolated	180	10	7	



TABLE III
RESULTS OF PENETRATION TESTS

Material	Dynamic Hardness Coefficient P_0 (MPa)	Work Hardening Exponent, η	Kink Depth $\frac{1}{2}$ (mm)	Ratios of Kink Depth	
				Measured	Predicted
A	340	0.36	0.6	1.33	1.21
B	390	0.37	0.55	1.22	1.19
C	530	0.45	0.45	1	1



TABLE IV
MATERIAL CONSTANTS USED TO MODEL
GLASS, BUNDLE AND MATRIX

Property	Material	Glass	Bundle	Matrix
Equation of State Constants:				
ρ_0		2.5 g/cc	1.87 g/cc	1.87 g/cc
A		34 GPa	25 GPa	4.2 GPa
B		2 GPa	0	0
Elastic Constants:				
$\nu_{r\theta}^*$		0.22	0.18	0.18
ν_{rz}^*		0.22	0.18	0.18
$\nu_{\theta r}^*$		0.22	0.03	0.18
E_{rr}^*		62 GPa	8.0 GPa	8.0 GPa
G_{rz}		25 GPa	21 GPa	3.4 GPa
Yield Constants:**				
σ_{y1}^0		400 MPa	$(\sigma_y)_{zz} = 800 \text{ MPa}$	17 MPa
σ_y		12 GPa	$(\sigma_y)_{rr} = 17 \text{ MPa}$	0
U_m		1.9×10^{10} ergs/g		7×10^{10} ergs/g
Tensile Failure Constants:				
$\hat{\sigma}_{zz}$		100 MPa	2 GPa	90 MPa
$\hat{\sigma}_{rr}$			90 MPa	
$\hat{\sigma}_{\theta\theta}$			90 MPa	

*Specified only for anisotropic material
**Yield in shear for isotropic materials. Failed materials have zero yield strength.



FIGURES

- Figure 1 A schematic diagram indicating kink formation in (a) longitudinal bundles and (b) lateral bundles.
- Figure 2 The apparatus used for constrained compression tests: (a) schematic of load application to sample, (b) an overview of the test fixture, (c) the sample and compression blocks.
- Figure 3 A kink formed just above the yield stress in a constrained compression test.
- Figure 4 A typical load/deflection curve obtained in a constrained compression test.
- Figure 5 Kink initiation stresses in the longitudinal bundles for the five materials listed in Table I.
- Figure 6 Kink initiation probabilities at a constant of 15 MPa for each of the five materials.
- Figure 7 The kink strength distribution $g(S_k)$ plotted as a function of the strength level S_k .
- Figure 8 Damage in the longitudinal bundles in material C created by a 3 mm diameter penetration.
- Figure 9 Damage in the lateral bundles in material C created by a 3 mm diameter penetration.
- Figure 10 Scanning electron microscope overview of the crater in material A at velocities of 4,000 and 6,000 ms^{-1} .
- Figure 11 Kinking in longitudinal bundles in material C impacted at 6,000 ms^{-1} : (a) section through impact center, (b) section adjacent to impact center.
- Figure 12 Kinking in longitudinal bundles in material B on sections through impact center: (a) 4,000 ms^{-1} , (b) 6,000 ms^{-1} .
- Figure 13 Kinking in longitudinal bundles on section through impact center at 6,000 ms^{-1} : (a) material D, (b) material E.
- Figure 14 Kinking in longitudinal bundles in materials A and B at the extremities of the kink zone indicating: (a) an unusual mode of kinking at the corners of out-of-plane lateral bundles, (b) kink initiation at a bundle/matrix void, (c) kink initiation at intrabundle voids.



- Figure 15 Kinking in lateral bundles in material C impacted at $6,000 \text{ ms}^{-1}$.
- Figure 16 The depth of kinking in the longitudinal bundles for 1 mm stress projectiles, as a function of the impact velocity.
- Figure 17 The extent \hat{x} of kinking in the lateral bundles.
- Figure 18 The scheme used for the numerical computation of kinking: (a) the cylindrical bundle impacted axially by the glass sphere, (b) the grid used for the computation.
- Figure 19 The time dependence of the interface stress predicted by the calculation.
- Figure 20 The time dependence of the stresses developed in the bundle at two distances z below the surface.
- Figure 21 The development of kinks within the bundle during the penetration process.
- Figure 22 A typical bundle inhomogeneity and the parameters used to estimate the fiber curvature.
- Figure 23 The displacement in the longitudinal, z , and lateral, x , directions predicted by the elastic/plastic pressurized cavity solution for an infinite solid (small x, z) and the elastic solution for a half space (large x, z), indicating possible interpolations.
- Figure 24 The curvature of lateral bundles beneath the penetration zone; also shown are the regions of axial compression and tension.

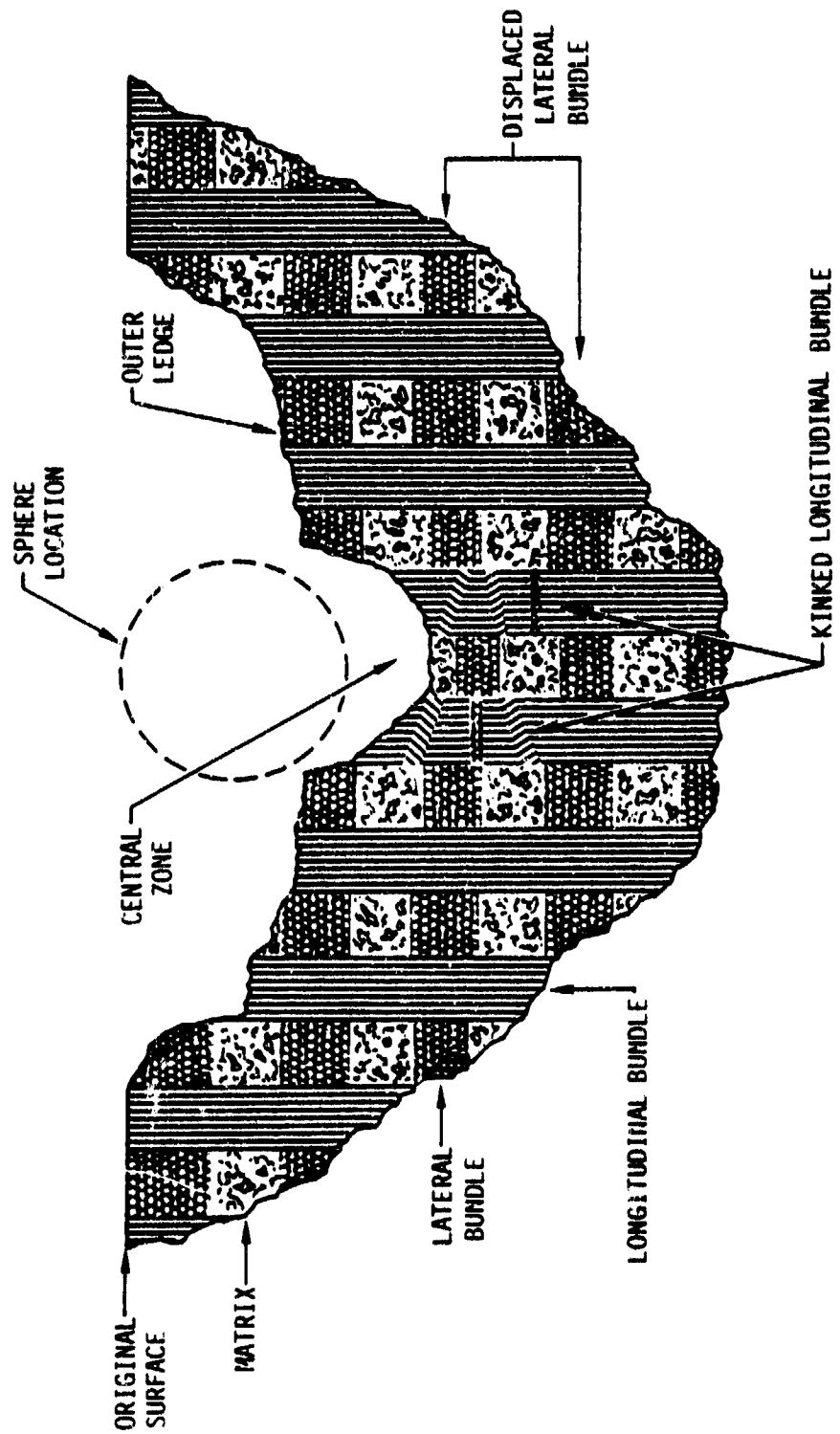


Fig. 1a

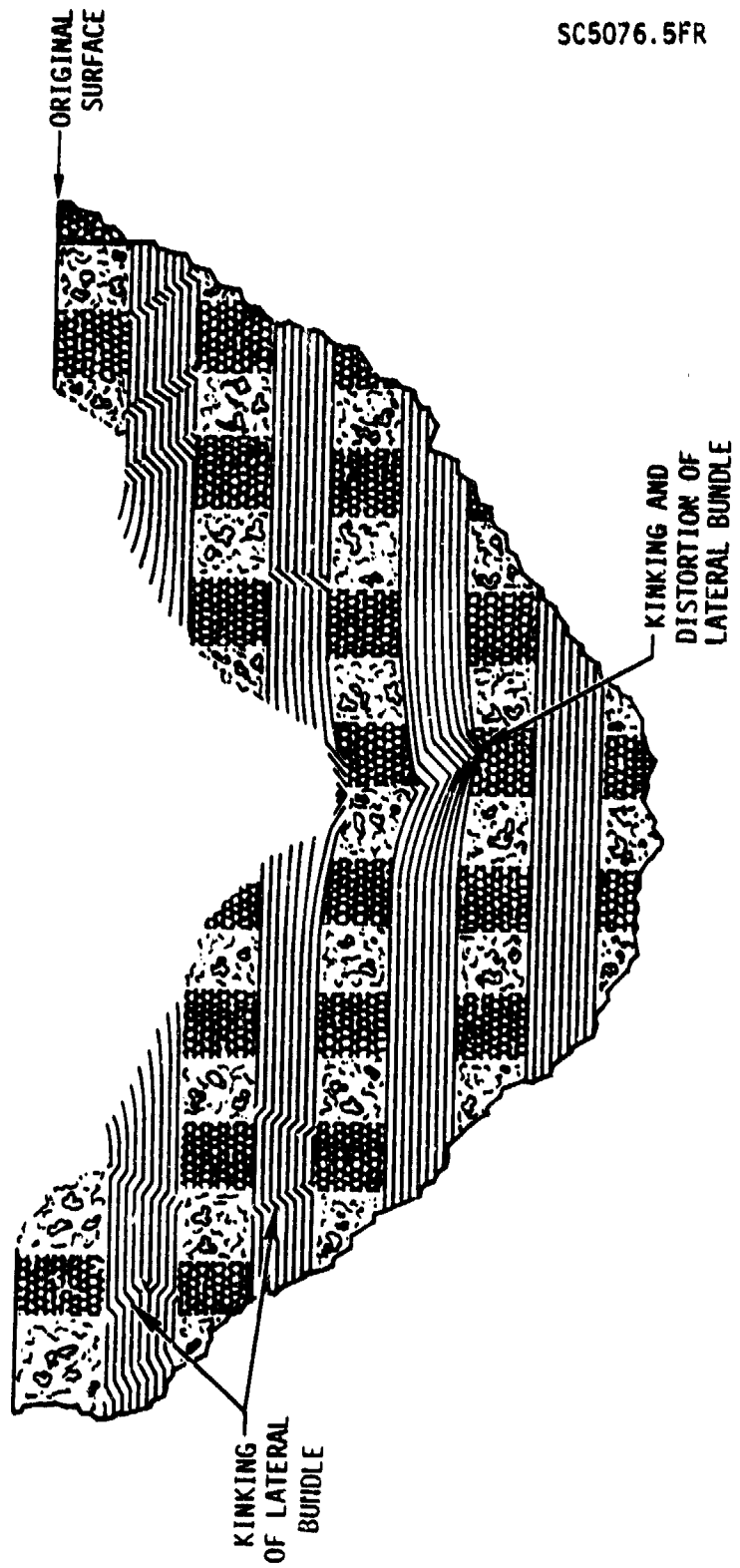


Fig. 1b



a

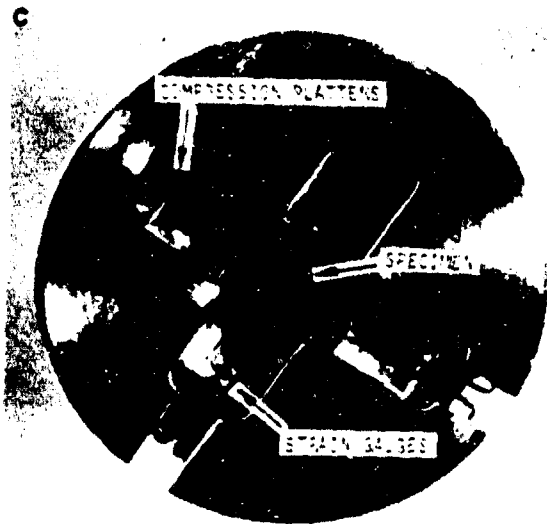
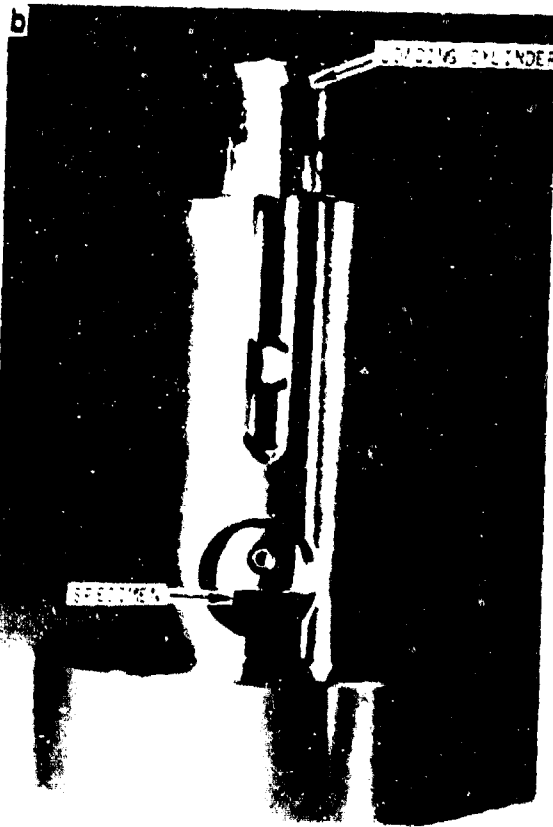
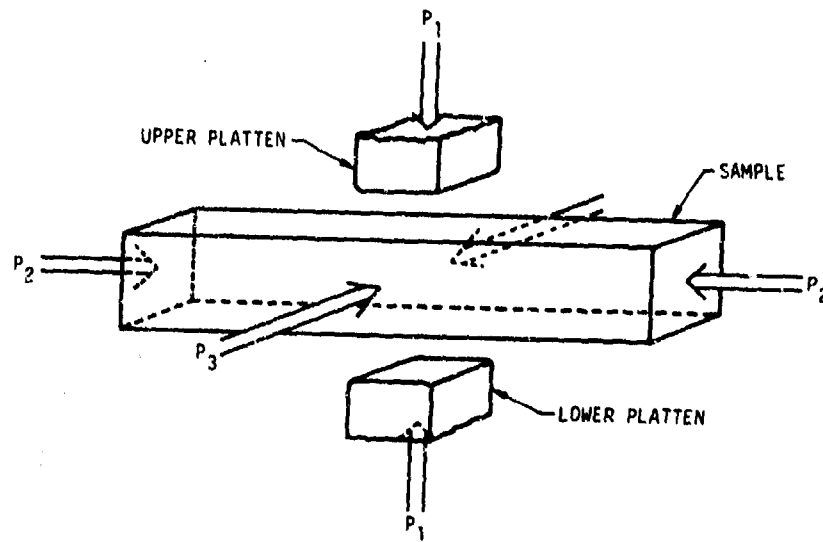


Fig. 2



Rockwell International
Science Center

SC5076.5FR



Fig. 3



SC5076.5FR

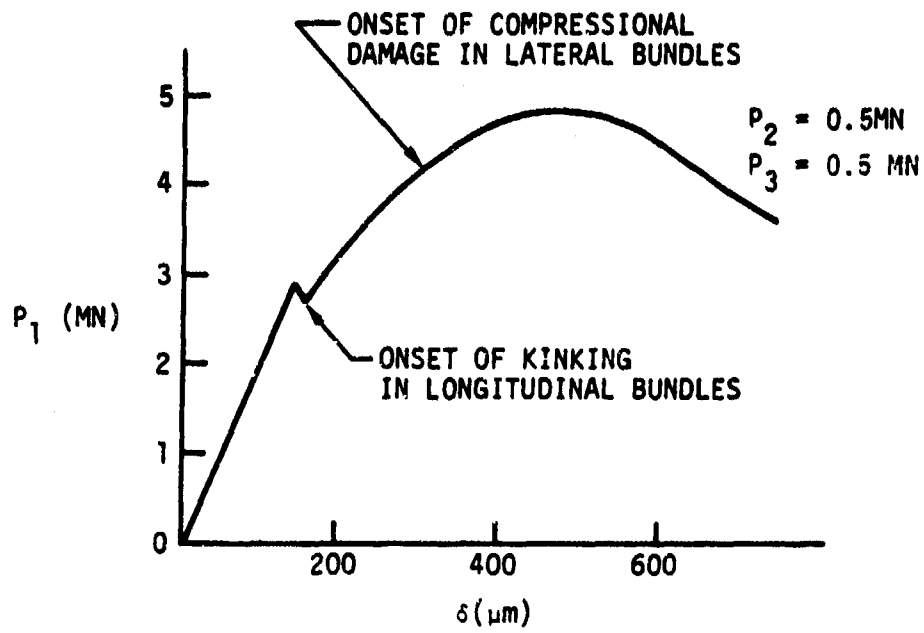


Fig. 4



SC5076.5FR

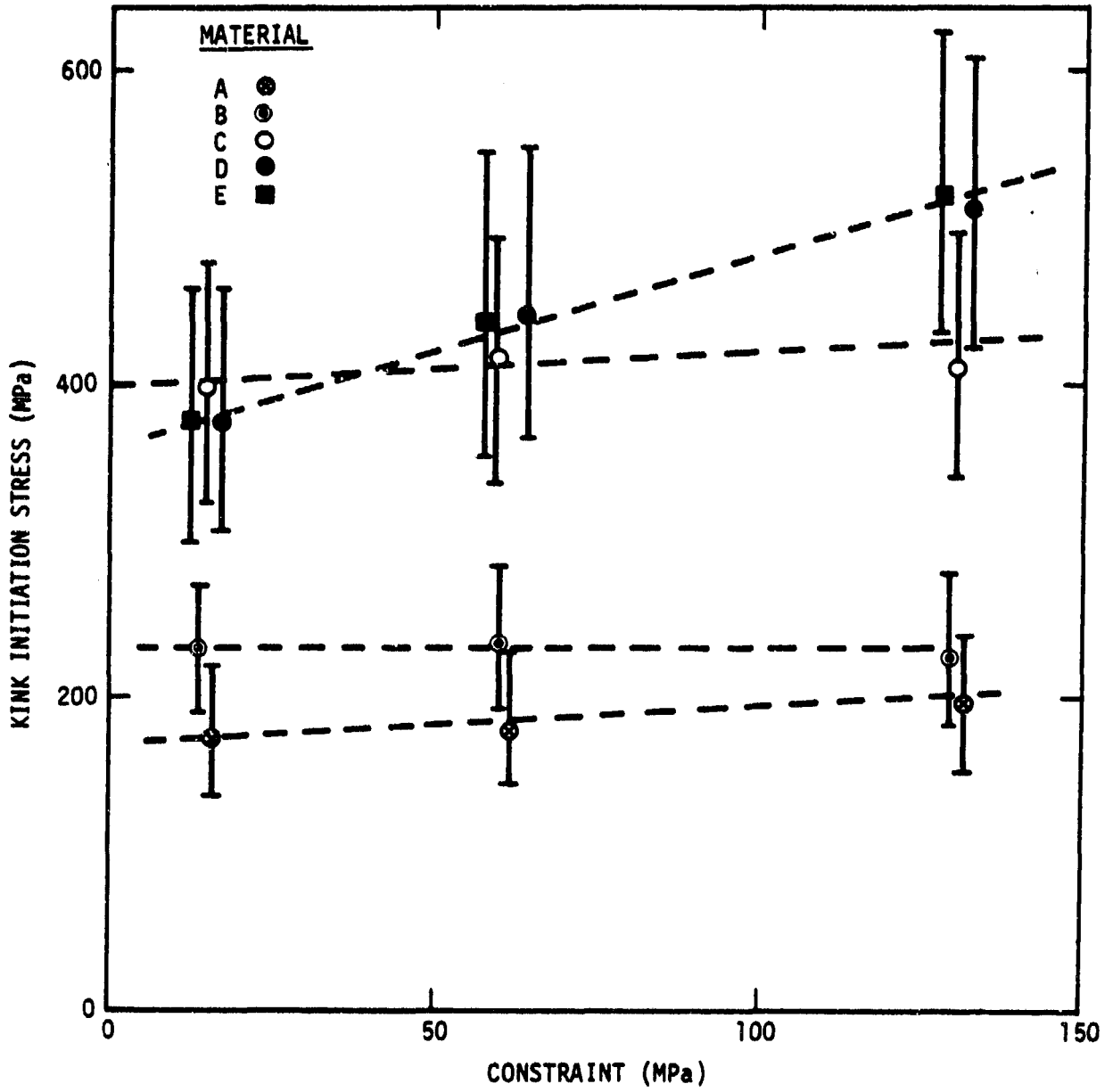


Fig. 5



SC5076.5FR

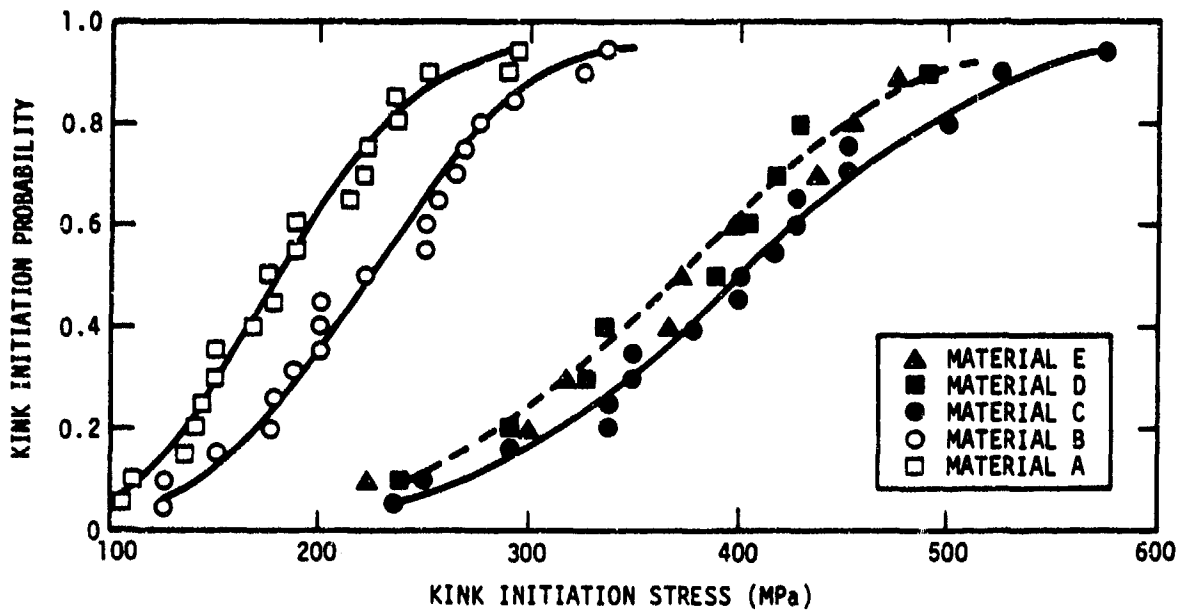


Fig. 6



SC5076.5FR

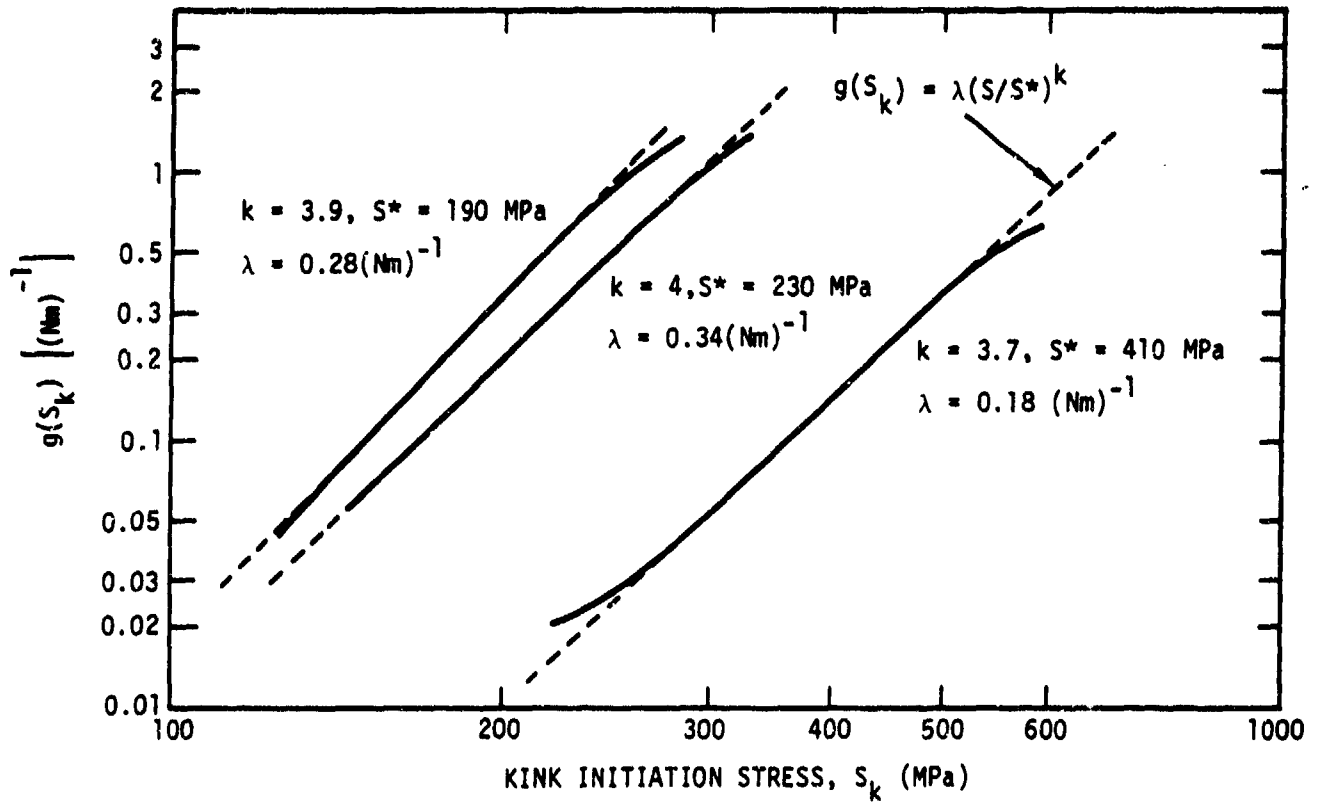


Fig.7



SC78-1253

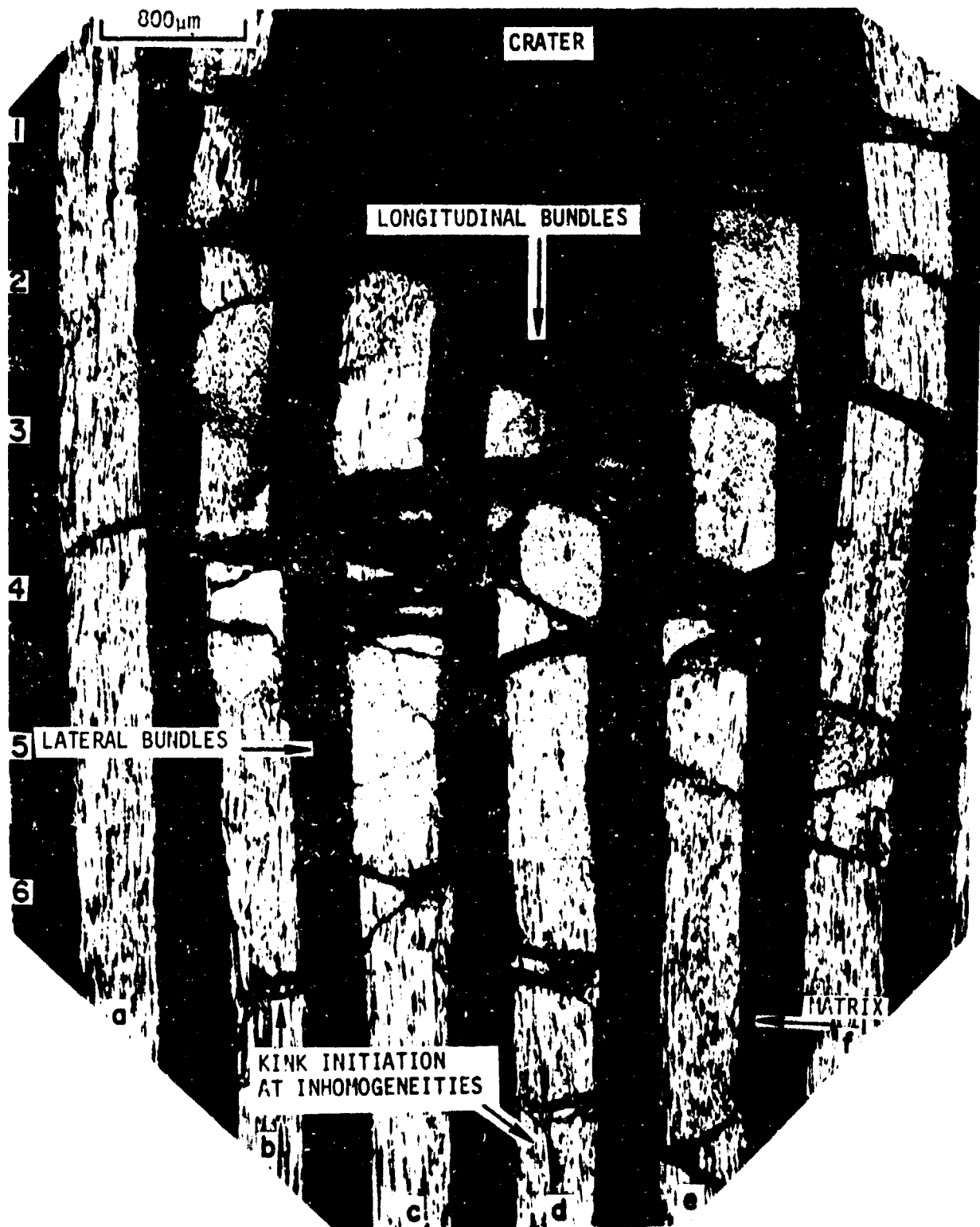


Fig. 8



Rockwell International
Science Center

SC5076.5FR

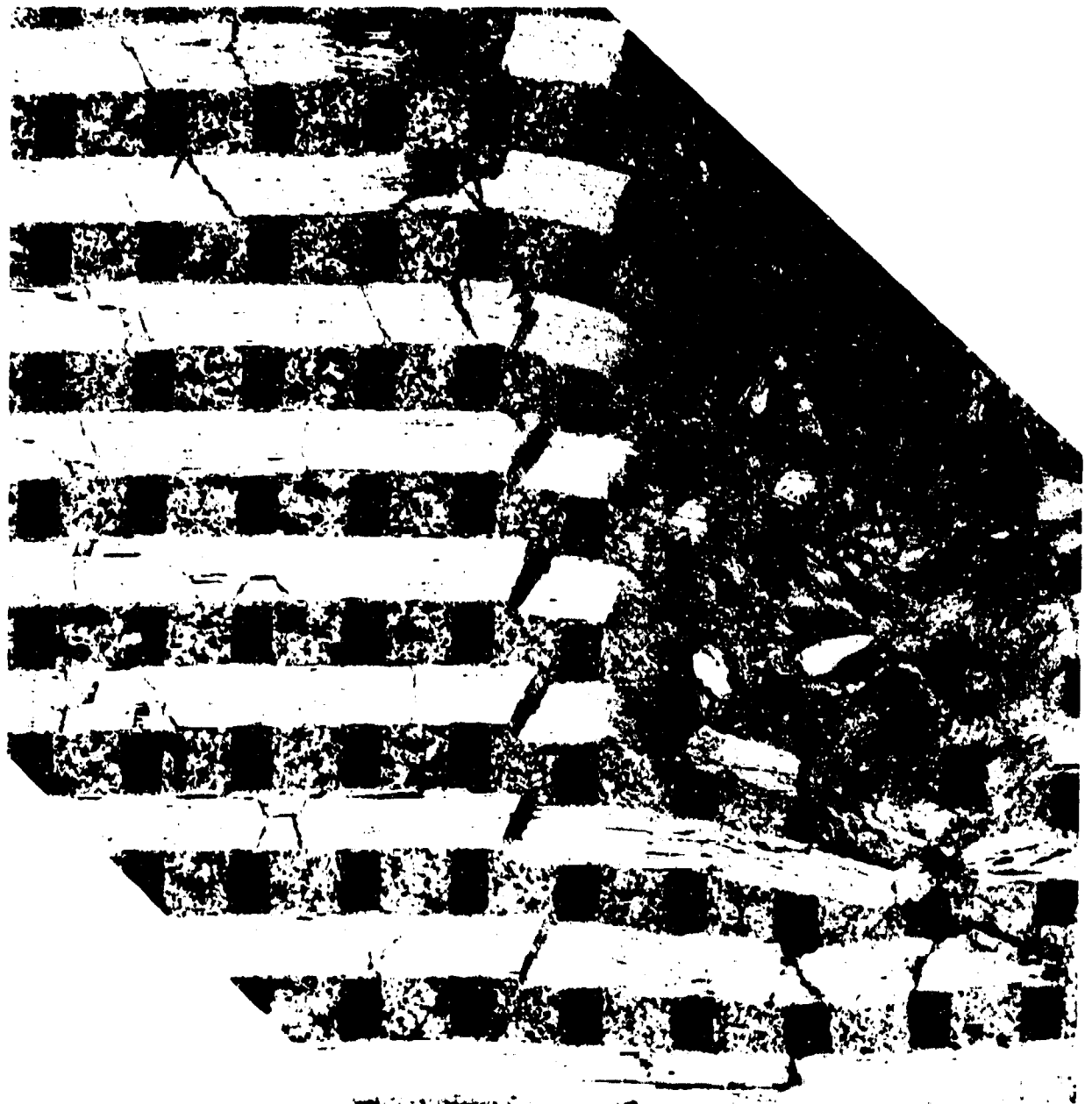


Fig. 9

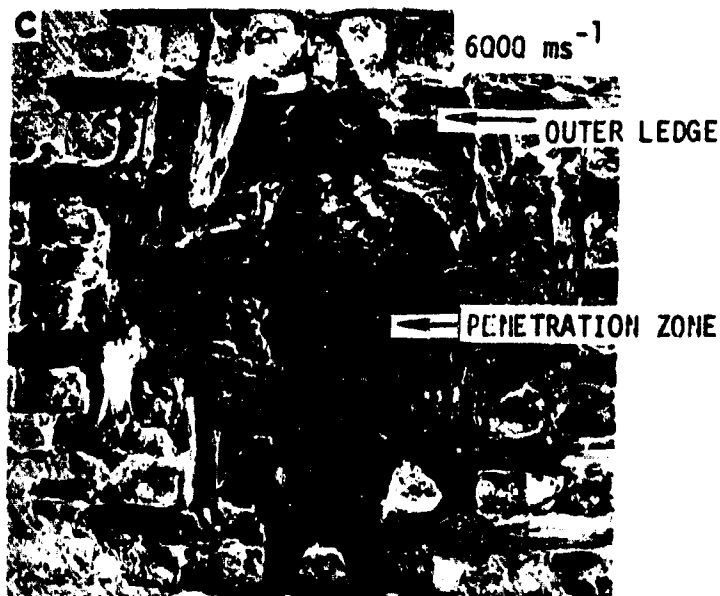
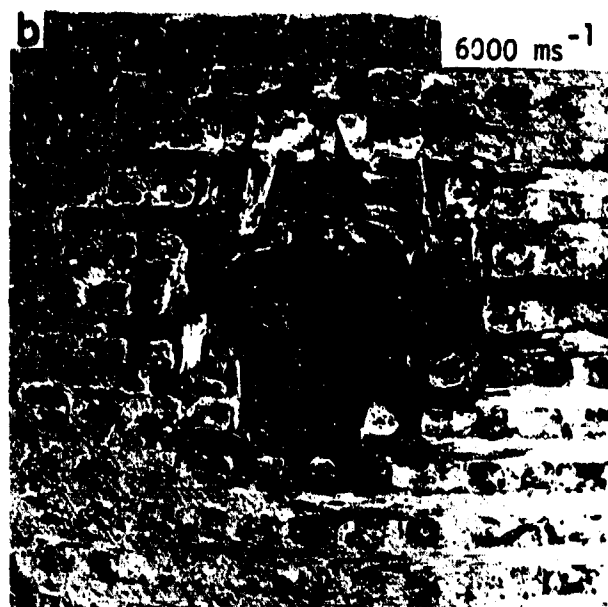
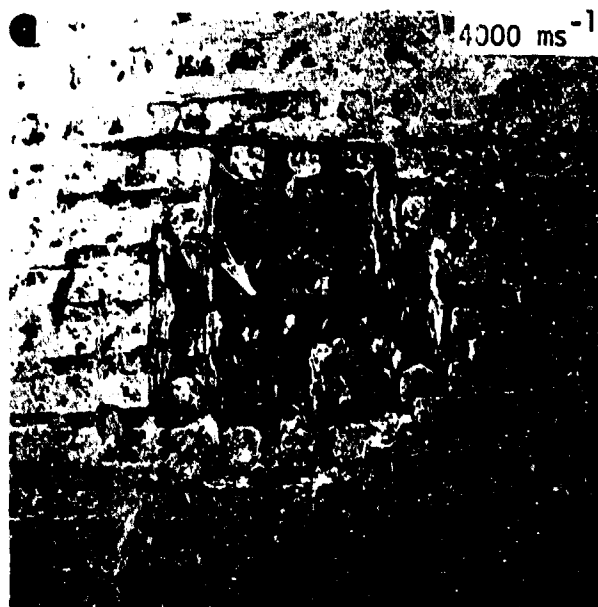


Fig. 10



SC5076.5FR



Fig. 11



Rockwell International
Science Center

SC5076.5FR

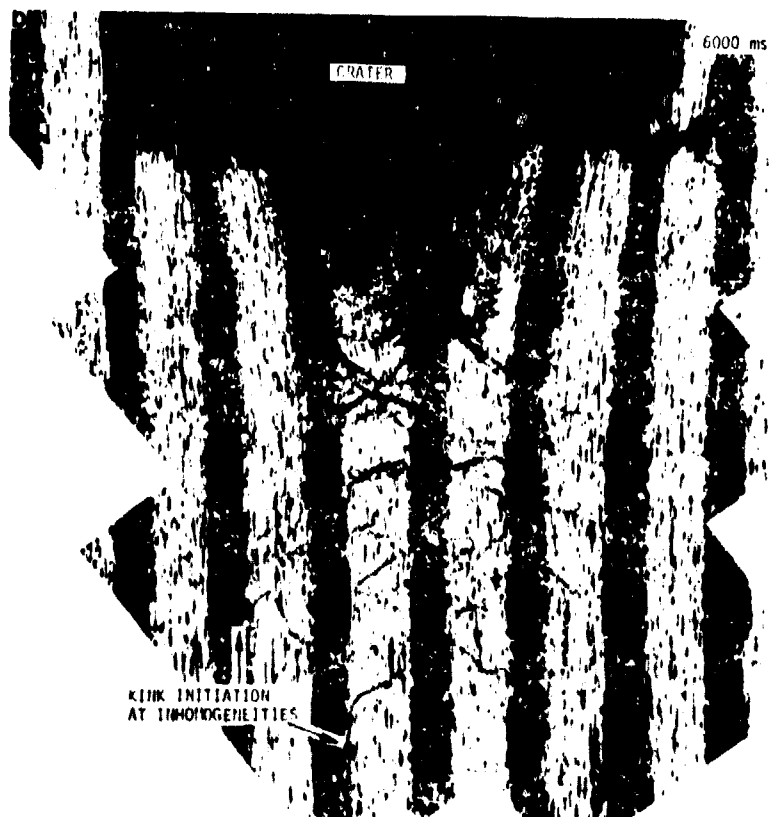
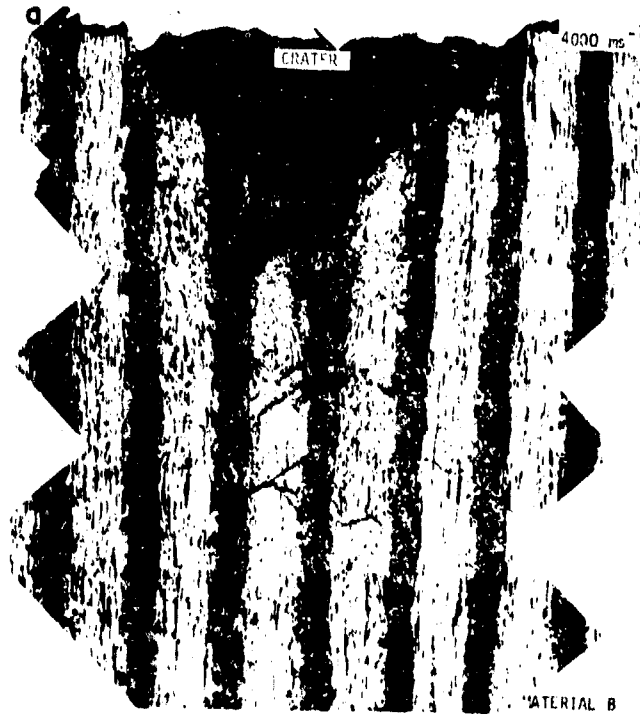


Fig. 12



SC5076.5FR



Fig. 13



Fig. 14

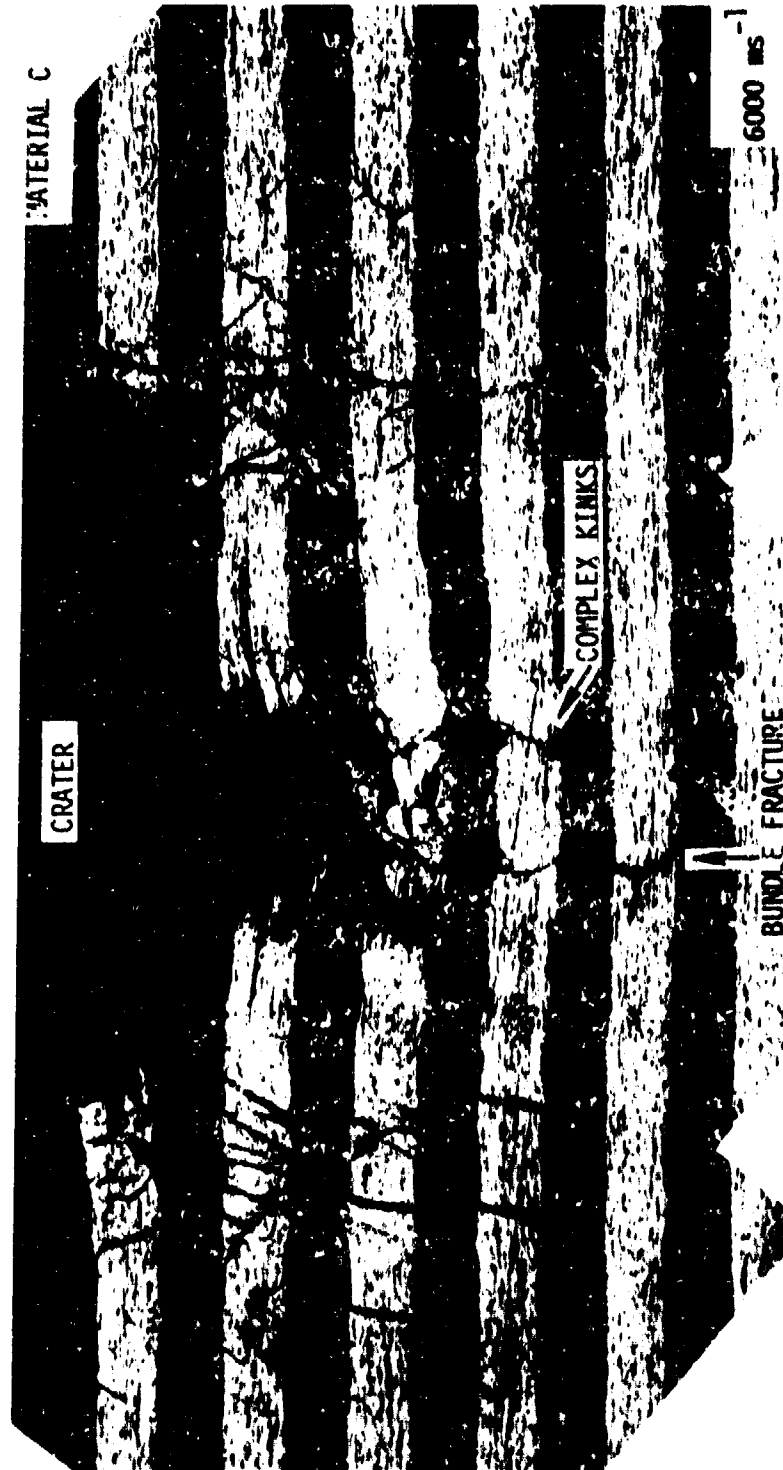


Fig. 15



SC5076.5FR

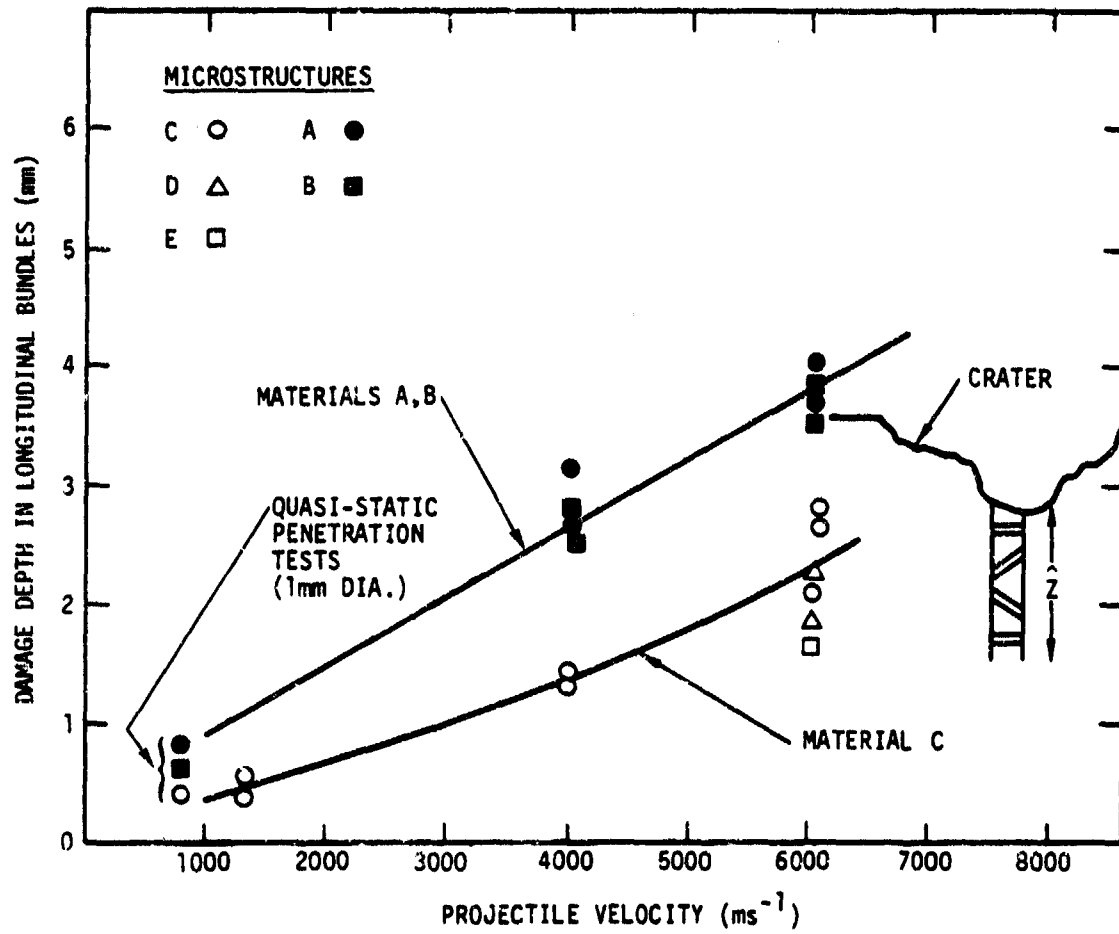


Fig. 16



SC78-1250



SC5076.5FR

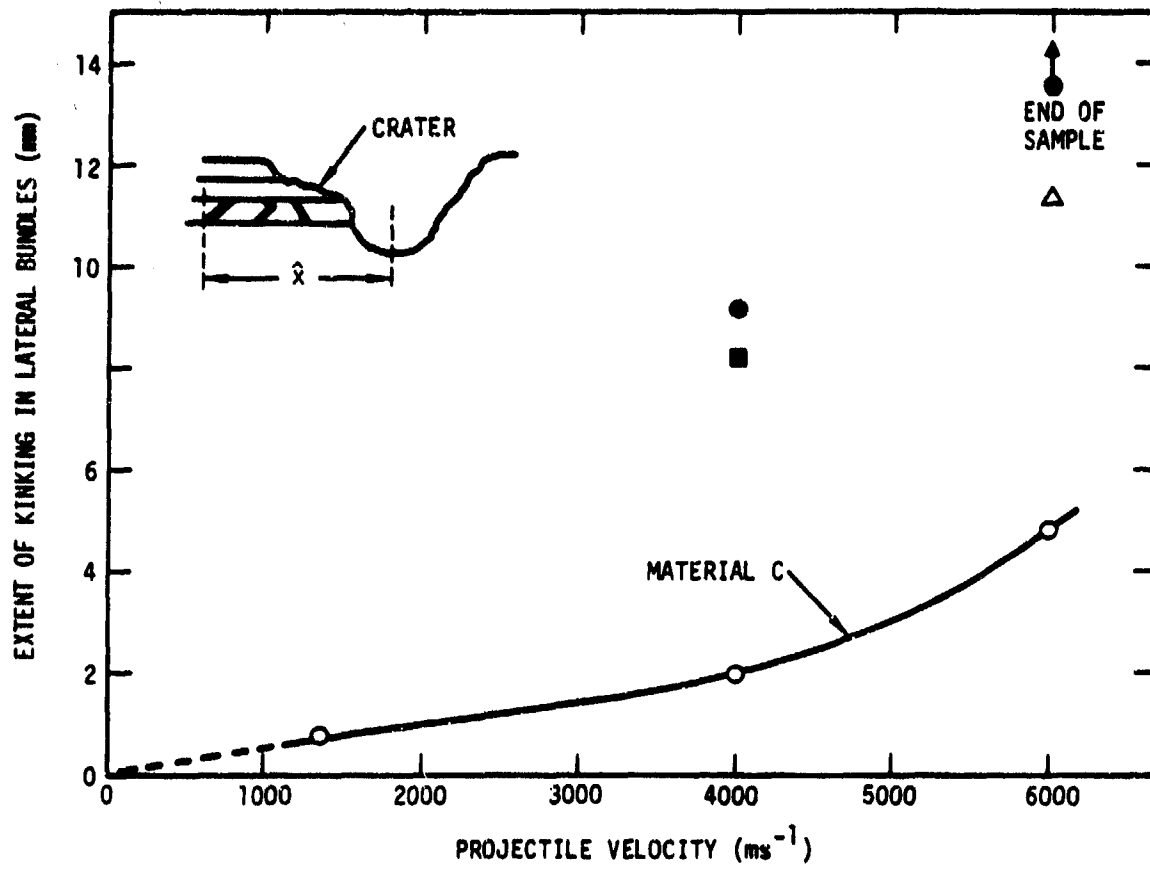


Fig. 17



SC78-1254-A



SC5076.5FR

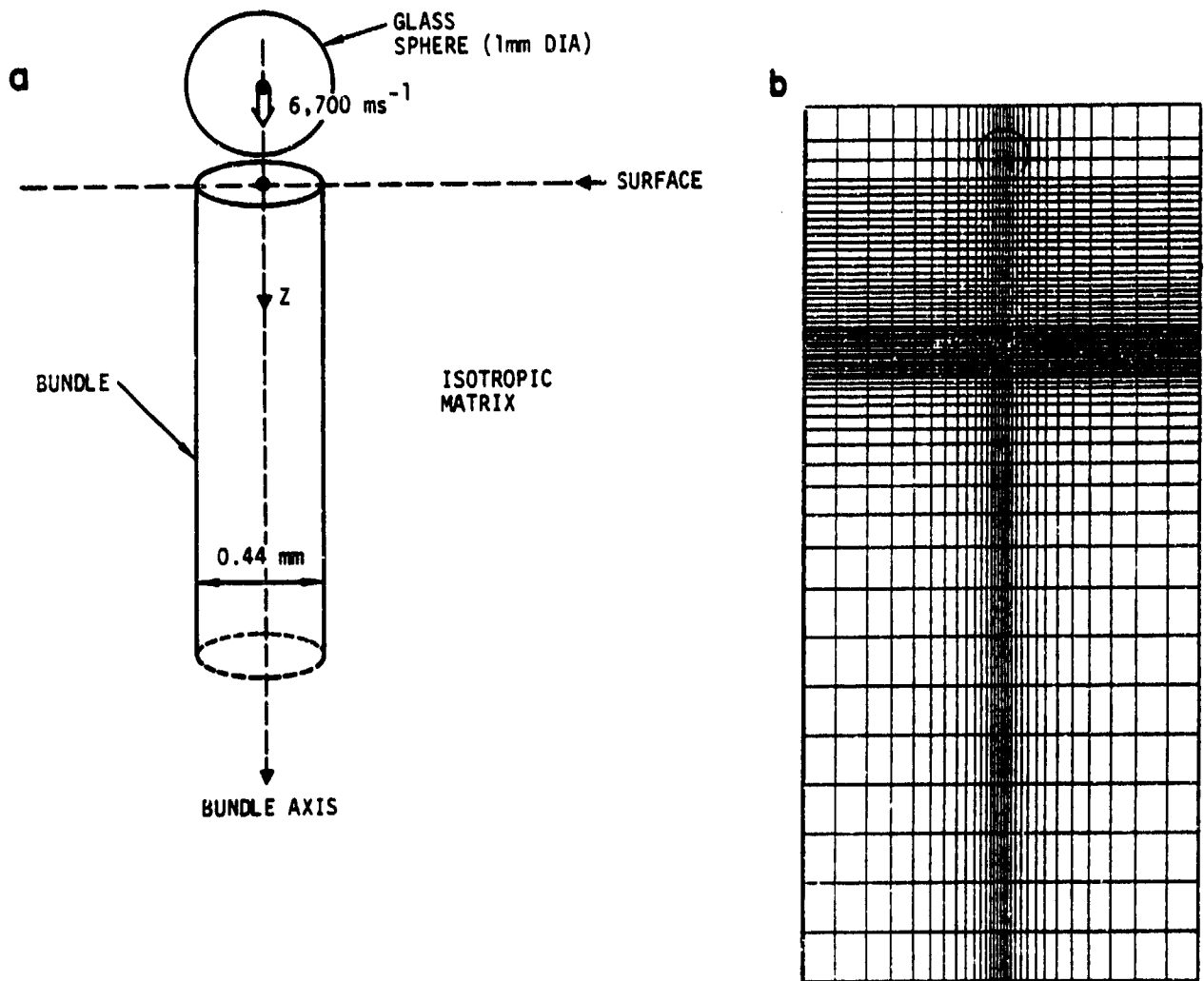


Fig. 18

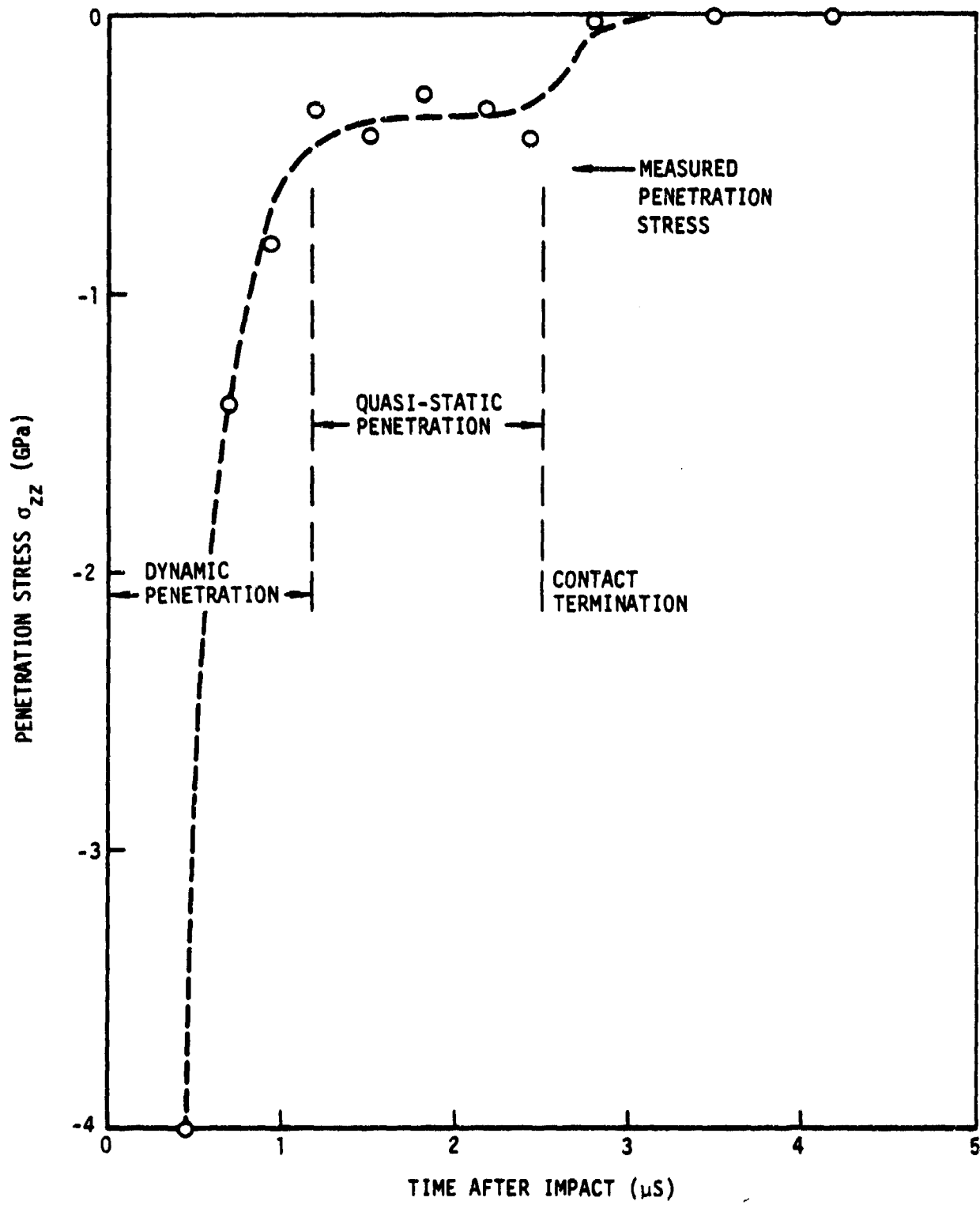


Fig. 19

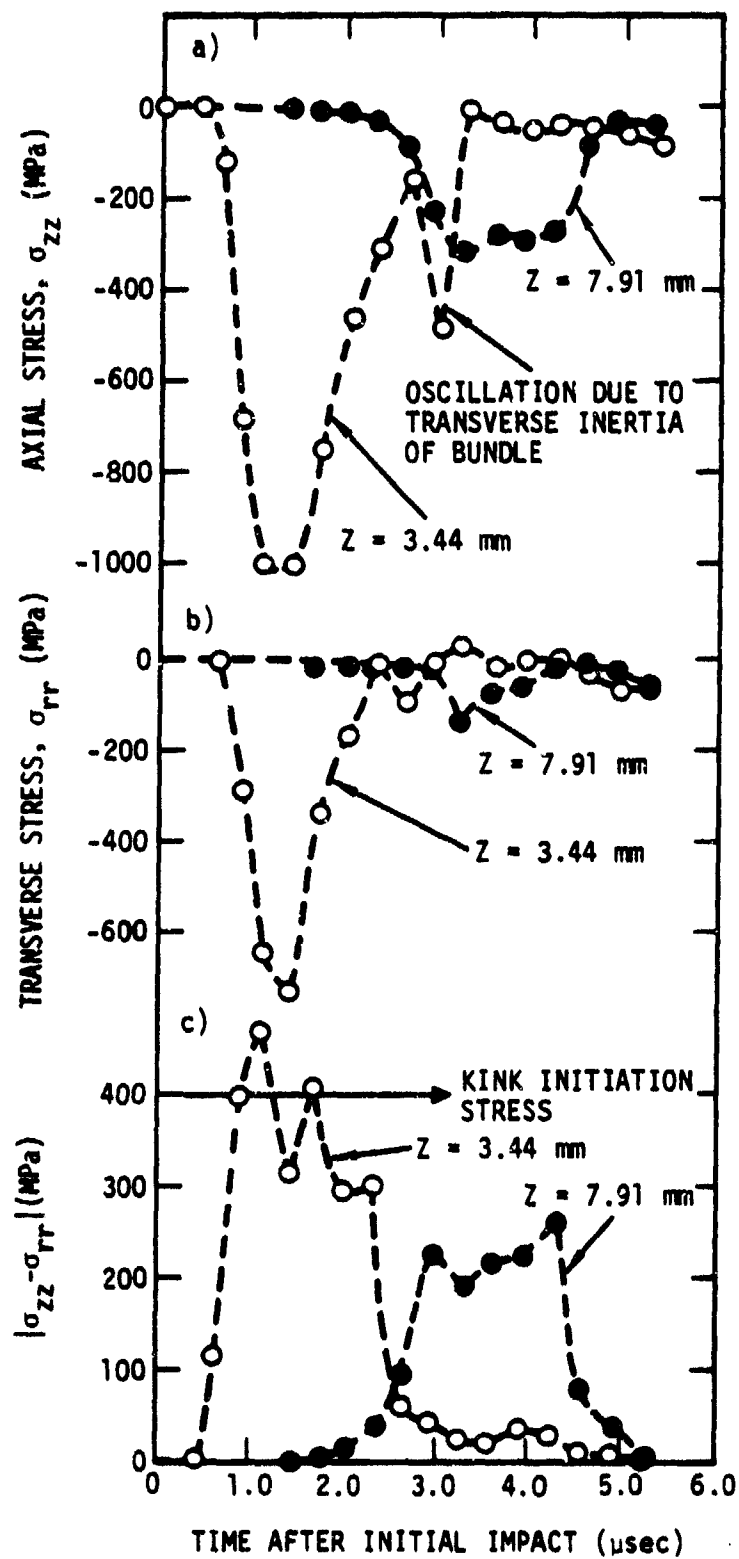
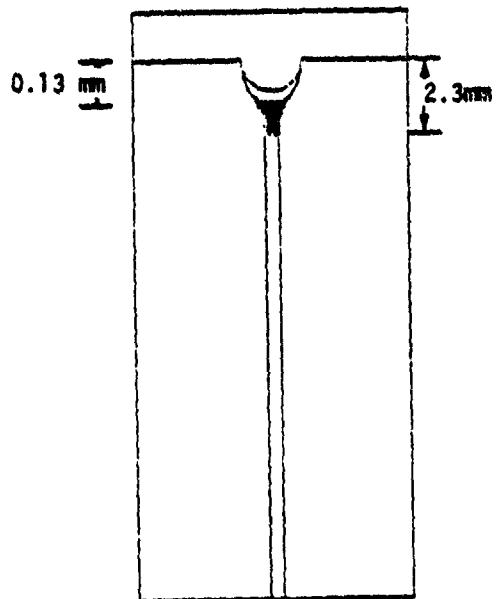


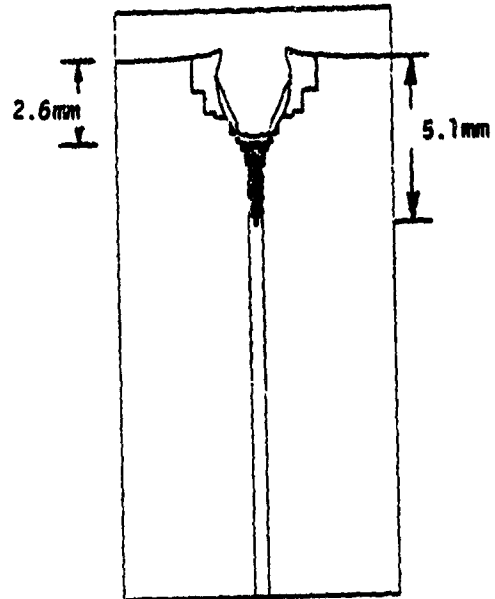
Fig. 20



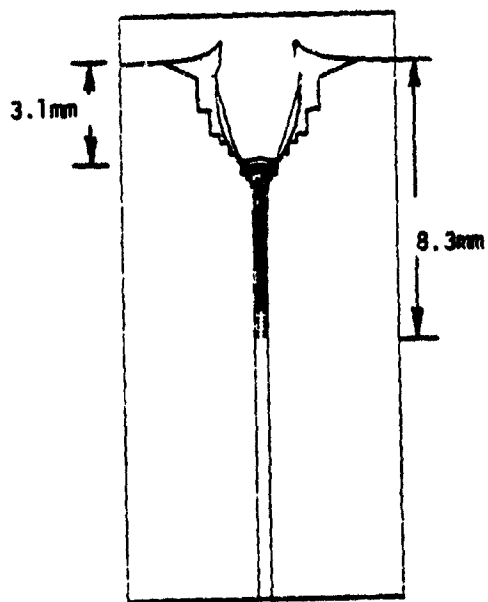
SC5076.5FR



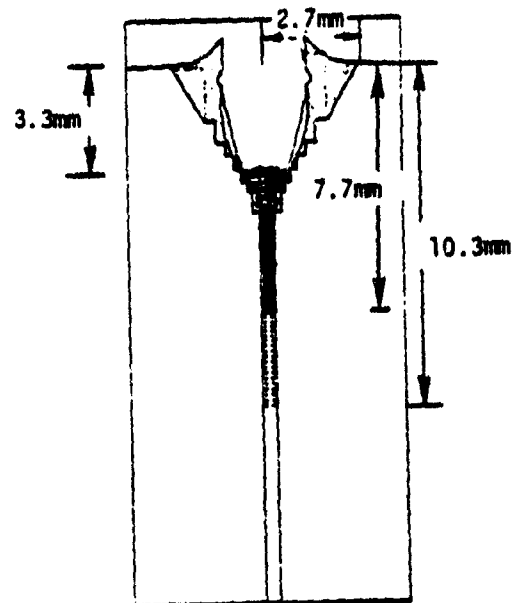
Time = 0.43 μ s



Time = 1.68 μ s



Time = 3.54 μ s



Time = 5.20 μ s

Fig. 21



SC5076.5FR

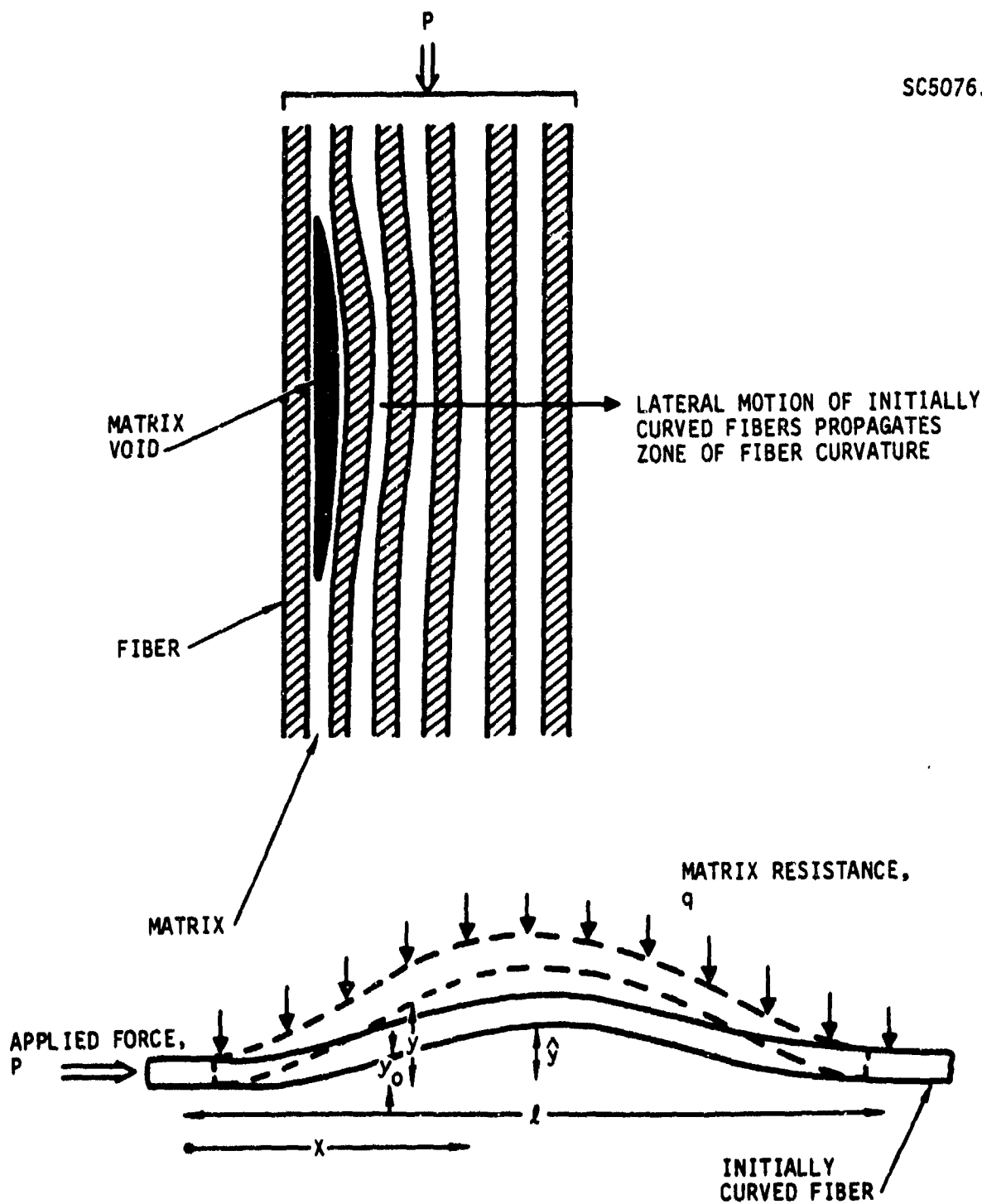


Fig. 22





SC5076.5FR

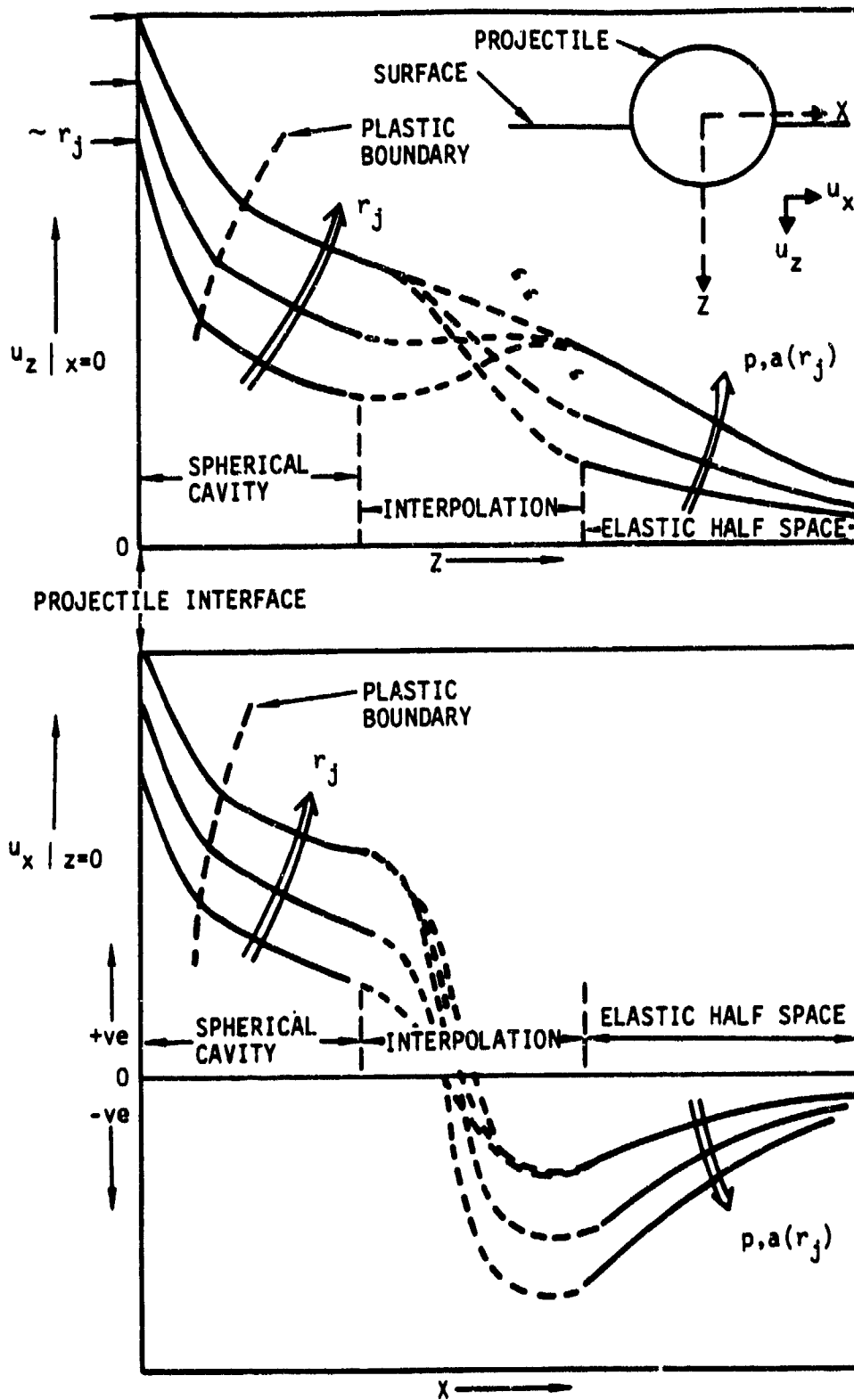


Fig. 23



SC5076.5FR

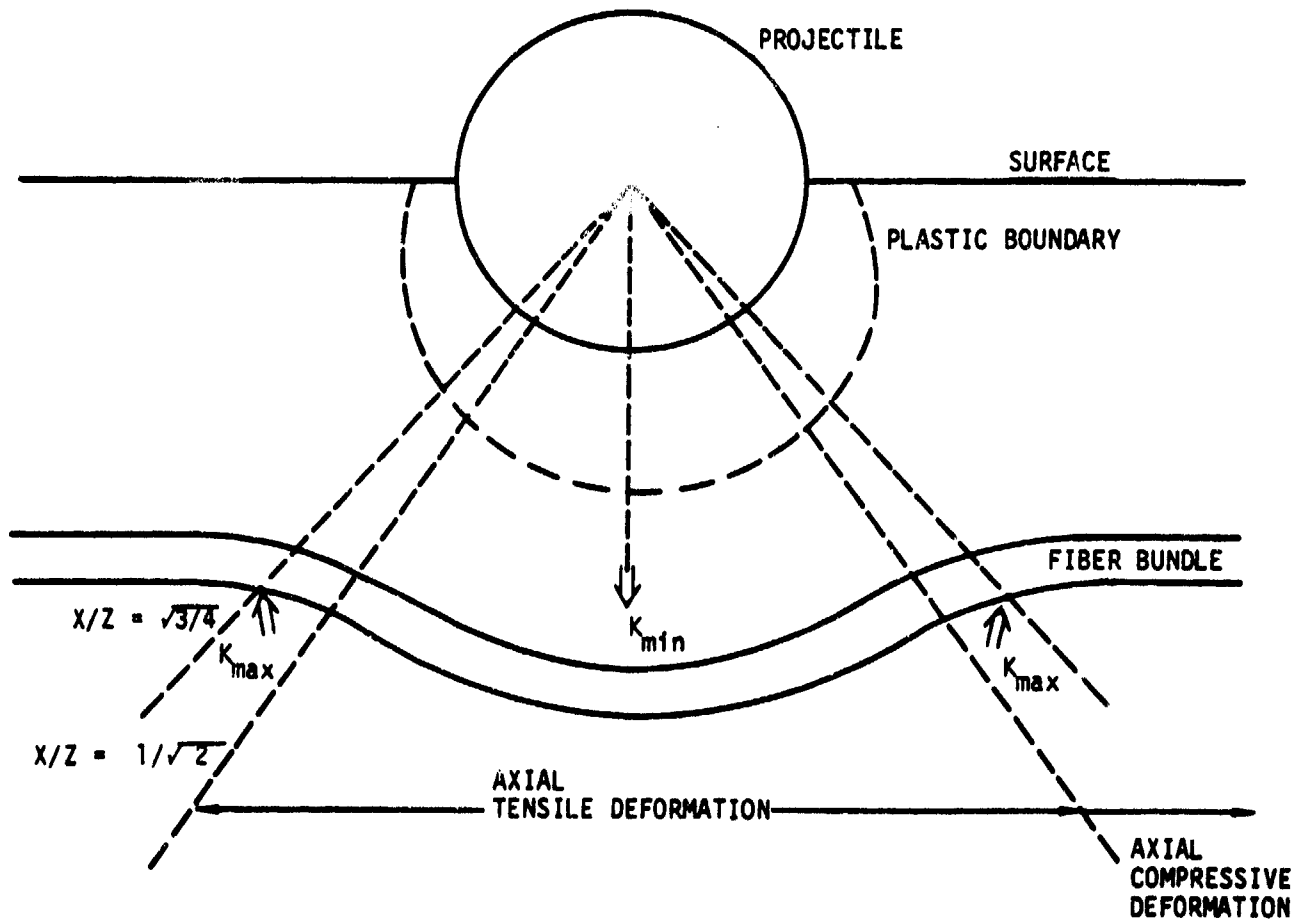


Fig. 24

 SC78-1249